

Fig. 32. Effect of the sintering atmosphere on the phase evolution and microstructure of sintered BT ceramics. Variation of the density as (a) a function of the applied current in UHS, and (b) a function of temperature, different hold time, and atmosphere in FF and P-SPS [113]. Raman and SEM analysis of the samples sintered using (c-d, g-l) UHS in different atmospheres, (e, m-o) P-SPS, and (f, p-r) FF [113].

Reproduced from Ref.: (a-r) [113], with permission from John Wiley and Sons.

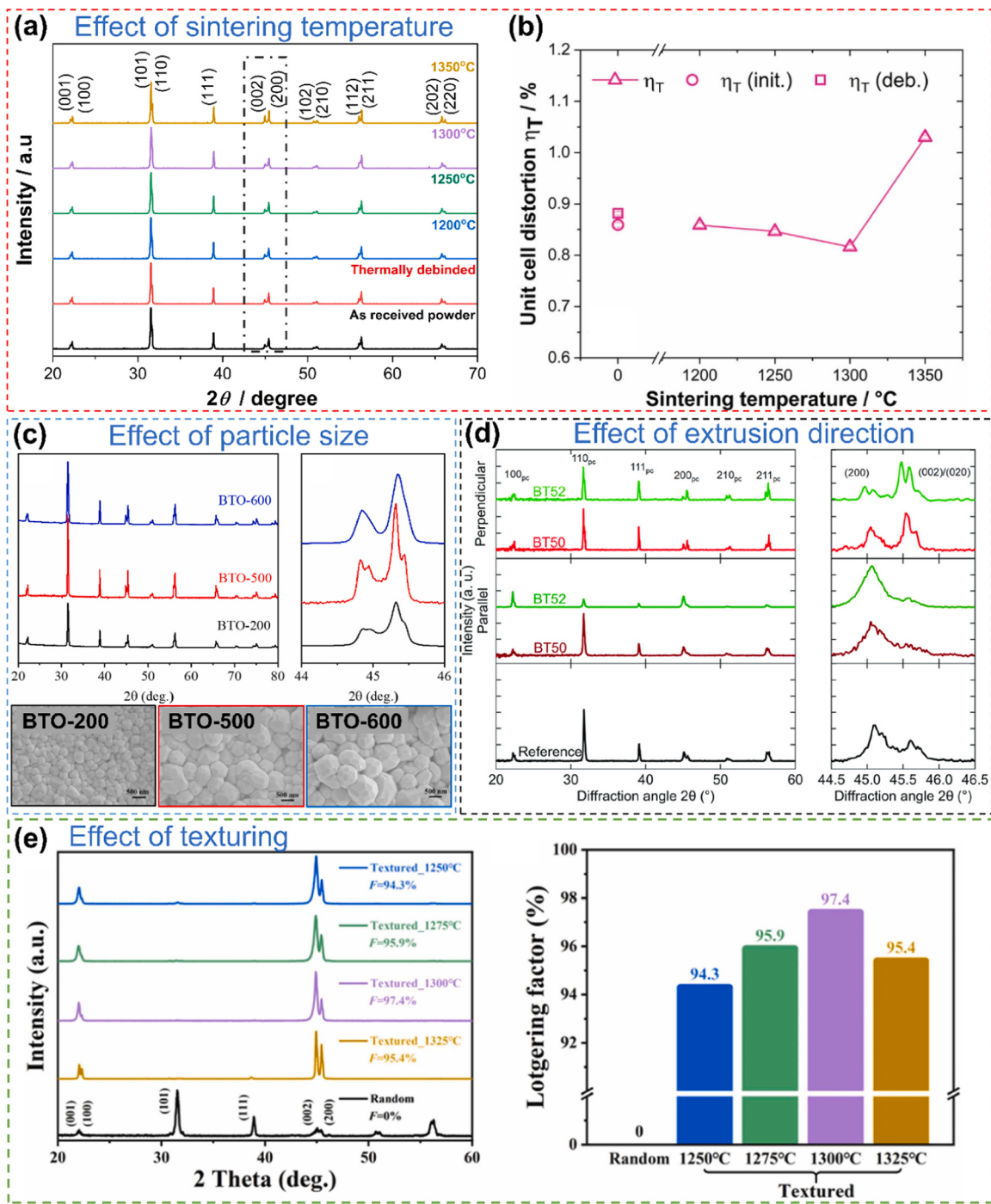


Fig. 33. Effect of sintering temperature, initial particle size, extrusion direction, and alignment on the XRD. XRD patterns of: (a) Sintered BT samples at various temperatures. The reflection at 45° has been marked with black colour and the corresponding unit cell distortion is shown in (b) [113], (c) Sintered BT ceramics with three different particle sizes; corresponding SEM images illustrating the diffraction patterns are provided below [147], and (d) Sintered BT samples measured in parallel and perpendicular to the extrusion direction [70]. (e) XRD patterns, and (f) Lotgering factor (F) values for both randomly oriented and textured BT ceramics sintered at different temperatures [163].

Reproduced from Ref.: (a-b) [113], (c) [147], and (e-f) [163], with permission from Elsevier. (d) [70], Open access article distributed under the terms of the Creative Commons CC BY license.

decrease in density as well as shrinkage (Fig. 34(a)) with precipitation of impurity phases (evidenced by XRD) and abnormal grain growth (Fig. 34(d)). The addition of CuO resulted in a shift of the reflection positions to lower 2θ angles [184] due to the larger ionic radius of Cu^{2+} compared to Ti^{4+} and Zr^{4+} , leading to lattice expansion. A similar reflection shift has been observed for substituting Ti^{4+} with Sn^{4+} in BT ceramics [167]. The decrease of the 200 reflection splitting (at $20 = 45^\circ$)

with increasing Sn^{4+} content, indicated the transformation of tetragonal to cubic symmetry.

In a recent study, authors have employed a mixture of copper oxide (CuO) and bismuth oxide (Bi_2O_3) as a sintering aid to induce liquid phase sintering [162]. It was found that the addition of the sintering aid increases the density (from 91 % to 93 %) and the Lotgering factor to about 58 %. In contrast, the Lotgering factor was only 2 % when only

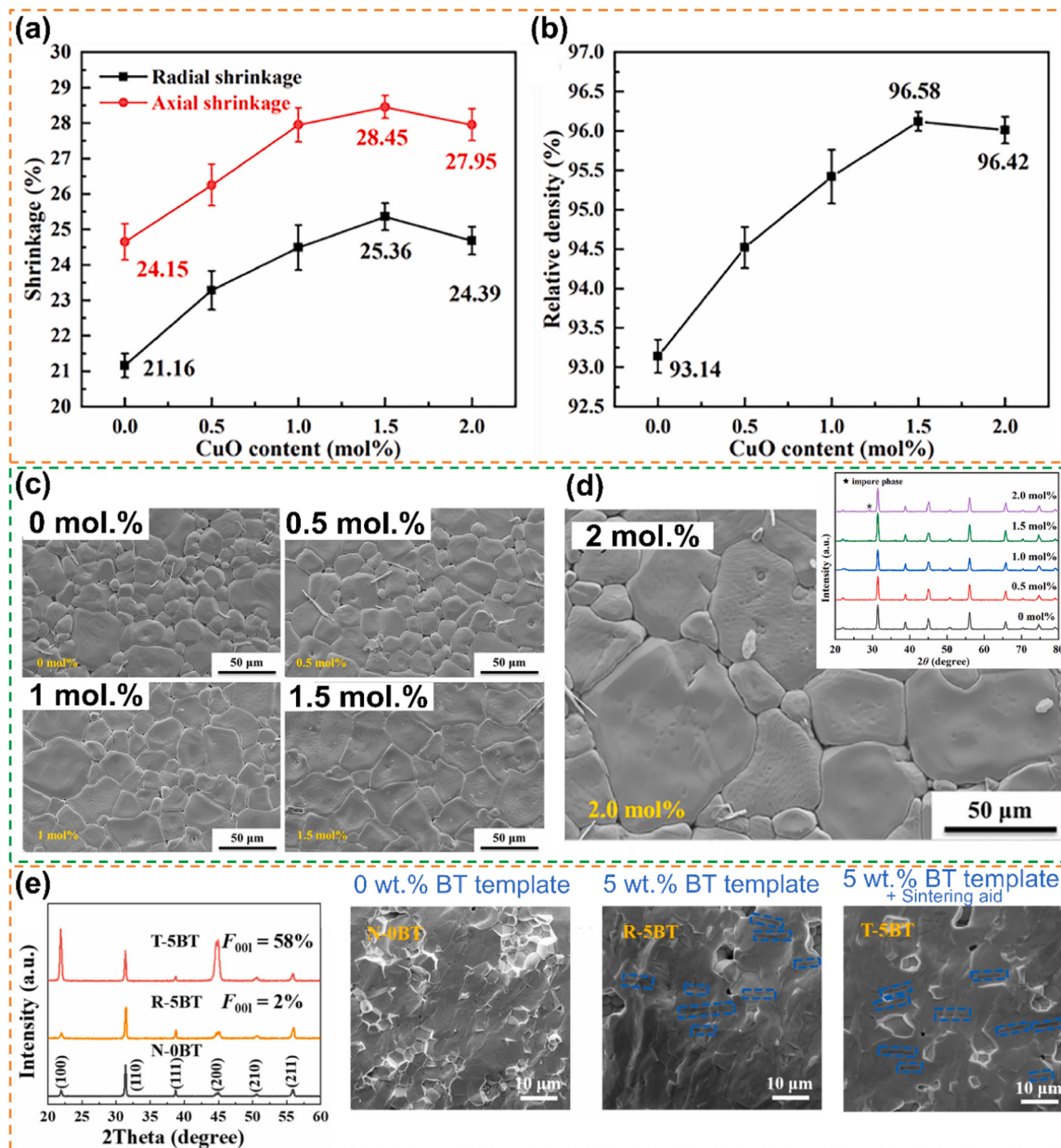


Fig. 34. Effect of sintering aid during sintering (a) Variation of shrinkage, and (b) Relative density of BCZT ceramics doped with varying amount of CuO. The corresponding microstructures are depicted in (c) [184]. (d) Abnormal grain growth with an excessive CuO content of 2 mol.% and the precipitation of unwanted secondary phases, as shown in the inset XRD pattern [184]. (e) XRD patterns of PMN-PT ceramics with BT templates and sintering aid, along with their corresponding SEM images [162].

Reproduced from Ref.: (a-d) [184], and (e) [162], with permission from Elsevier.

5 wt% of BT platelets were used without the sintering aid (Fig. 34(e)).

Usually, the permittivity (ϵ_r), which denotes the ability to store electrical energy, is measured as a function of frequency or temperature and shows maxima at phase transformation temperatures [86,139,146, 147,150,158,168,171,172,180]. Above RT for BT ceramics ϵ_r decreases with temperature (up to 75 °C) which is correlated to the orthorhombic-to-tetragonal phase transformation [70]. Similar phase transformation temperatures have been reported for several other compositions [80,149,180,184]. Some compositions even show two intermediate phase transformation temperatures as reported for Sn-doped BT [167]. With a further increase in temperature up to the Curie temperature (T_c) the ϵ_r increases and shows a maximum at T_c [146,147,169,180]. A similar temperature dependence behaviour is exhibited by d_{33} or the piezoelectric coefficient. However, at T_c (Tetragonal to cubic phase transformation), the value decreases sharply

to almost zero, denoting that the material no longer exhibits piezoelectric properties. Therefore, higher Curie temperatures are desired, so that the material can retain its piezoelectric properties at higher temperatures. For instance, the T_c of PZT (220 °C) [94] and KNN (230 °C) [180] are much higher than those of BT (130 °C) [70] and BCZT (86–88 °C) [51]. This suggests that PZT and KNN are better candidates when high temperature applications are necessary.

The T_c is a material specific property and is highly sensitive to various factors such as interfacial strain, defect density and internal stresses, all of which depend on the microstructural features of the sintered ceramics. For BCZT ceramics, T_c decreases slightly with increasing sintering temperature or grain size. This is in good agreement with the fact that T_c varies inversely with grain size [51,223]. Conversely, an increase in the ceramic loadings (the grain size also increases) in the ink leads to an increase in T_c [151,224]. The authors reported that the increase is

attributed to the growth of the domains with increasing grain size, while small grain sizes in the range of nanometres can increase T_c [146,147]. The fine grain size at nanometer level contributes to the improvement of T_c due to increased grain boundary effects, stress and surface-to-volume ratio. Additionally, the presence of residual porosity after the debinding, as well as the use of pore-forming agents increases the phase transformation temperatures [80,145,150,172,173]. This can be attributed to the stress relaxation near the porosity [225]. Interestingly, the effect of texturing on T_c is complex and reported to result in both decrease and increase. In a recent study, where BT platelets were used in a PMN-PT matrix, T_c decreased after texturing due to the heterogeneous interface effects leading to interfacial stress between the platelets and the matrix [162]. In contrast, when both the matrix and platelets are of the same composition, T_c is reported to increase after texturing because of the decreased grain boundary effects and aligned grain growth [163]. In a recent study, authors reported that T_c of BT ceramics decreases with increasing Sn^{4+} doping concentration (as shown later in Fig. 41(a-b)) [167]. This is related to the distortion in the lattice by substitution of Ti^{4+} by Sn^{4+} .

Permittivity (ϵ_r) measurements are often accompanied by dielectric loss ($\tan\delta$) measurements. Dielectric loss represents the energy lost in ferroelectric domains when they move in response to an applied electric field. The $\tan\delta$ value increases with the frequency [146,147,150,171, 180]. This is due to the fact that higher frequencies cause dipoles to reorient themselves more frequently, which can lead to a greater loss of energy. Additionally, sintered piezoceramics with low density and high porosity exhibit increased loss [85]. The presence of porosity leads to more interfaces, scattering of charges and disruption of uniformity, all of which contribute to $\tan\delta$. The dielectric loss also exhibits a sharp rise at T_c [51,94]. The phase change could potentially result in frictions between the ferroelectric domains, leading to enhanced $\tan\delta$ [226]. Beyond the T_c , $\tan\delta$ continues to rise, indicating that the material's ability to store and dissipate electrical energy changes as it moves away from its phase transformation point [151].

When considering the dielectric and piezoelectric response of the sintered samples, several parameters must be considered. In our investigation, we have identified the key parameters that significantly influence the electrical response of the material. Before proceeding further, let us provide a brief overview of the related piezoelectric or ferroelectric behaviour, which will be often used in the subsequent discussions.

- Piezoelectric coefficient or d_{33} :** This value quantifies the electrical displacement generated per unit of the applied mechanical stress along the same direction of the electrical field. Higher d_{33} implies more efficient conversion of mechanical to electrical energy.
- Remanent polarization or P_r :** This value dictates the ability of the material to retain polarization in the absence of an electrical field. Polarization in this text refers to the alignment of the dipoles. Usually, the dipoles are randomly oriented in the absence of an electrical field. On applying an electric field, the dipoles are oriented in the direction of the applied field.
- Strain or S :** Strain represents the relative change in the dimension of the material when subjected to an external electrical field.
- Piezoelectric voltage coefficient or g_{33} :** This value quantifies the electric field (or voltage) generated in the same direction as the applied stress.
- Figure of merit (FOM):** This is a measure of overall efficiency of a particular device. It takes into account different piezoelectric coefficients, permittivity and mechanical quality factors.

(i) Effect of initial particle size

The particle size of powders plays a crucial role in determining their functional properties, particularly in piezoelectric and dielectric ceramics. At identical sintering temperatures, a powder with fine particles

exhibits high sinterability, leading to grain growth and a dense microstructure easily. This is because fine particles have a larger surface area to volume ratio, which enhances the mass diffusion promoting the sinterability and grain growth. Conversely, a powder with coarser particles shows limited grain growth with residual porosity due to incomplete sintering. Hence, finer particles should exhibit superior properties compared to coarser particles (Fig. 35(a-b)) [58,59]. In a recent study, authors employed different sintering temperature for different particle size of the initial powder [147,194]. For instance, a temperature of 1300 °C, 1320 °C, and 1330 °C was selected for powder of 200 nm, 500 nm, and 600 nm in size. The best properties were achieved for 600 nm powder as the grain size after sintering was around 875 nm [147]. According to Ma *et al.*, optimal functional properties were observed with a particle size of 1.5 μm, while finer particles (0.6 μm) caused micro-cracks in the sample, due to weak inter-layer adhesion [141]. Increasing the particle size to 1.5 μm led to a decrease in density, which negatively impacted the dielectric/piezoelectric properties.

The situation becomes complex with a multi-modal particle size distribution. For instance, properties in a bi-modal particle size distribution decreased with increasing volume fraction of the coarser particles [61]. However, piezoelectric characteristics peaked at equal fractions of particles of 100 nm and 400 nm (Fig. 35(c-d)). This can be attributed to better densification behaviour and optimal grain size (1.46 ± 0.277 μm). Several studies reported that better properties are achieved when the average grain size after sintering is close to 1 μm [16, 147,158]. In order to achieve a grain size of around 1 μm, the authors employed appropriate ratio (2:8) of fine and coarse powders [158].

To understand the peak value of properties, it is essential to consider the size of the domains and the configuration of the domain walls. In ferroelectric materials like BT, domains are regions where the electric polarization is uniformly aligned in a particular direction. These domains are separated by domain walls, which are boundaries where the polarization direction changes. Typically, the tetragonal phase of BT consists of two types of domains: anti-parallel 180° domains and perpendicular 90° domains [227]. In coarser grains (>10 μm), both types of domains are present as coarser grains provide more space to accommodate multiple domain configurations. Conversely, only 90° domain walls are dominant when the grain sizes are <10 μm. When the grain sizes are around 1 μm, the width of the 90° domains decreases [228]. Smaller grain sizes lead to smaller domains with higher domain wall densities, thereby increasing sensitivity to applied external fields or stress. However, well below 1 μm the domain wall mobility decreases significantly, resulting in lower properties [15,16,229].

BT ceramics exhibit optimal dielectric and piezoelectric properties at an average grain size of approximately 1 μm and a stoichiometric Ba/Ti ratio of 1 [229]. At this grain size range, the density and mobility of domain walls are maximized, enhancing the material's response to electric fields. This grain size range also minimizes the adverse effects of grain boundaries, which can pin domain walls and reduce their mobility in smaller grains. Maintaining a precise Ba/Ti ratio is equally crucial. A stoichiometric Ba/Ti ratio ensures minimal defects and secondary phases, which can degrade the material's properties. Ba deficiency (Ba/Ti < 1) leads to the formation of titanium-rich phases and oxygen vacancies, which pin domain walls and reduce the permittivity. Conversely, Ba excess (Ba/Ti > 1) introduces barium-rich phases and localized stresses, negatively impacting the dielectric and piezoelectric properties. It is worth noting that while an average grain size around 1 μm often results in high properties, it is not a straightforward conclusion. For instance, Sufiarov *et al.* reported that the best properties are achieved when the grain size of the sintered BT ceramic is 10 – 50 μm [194]. The functional properties of BT ceramics are quite complex and depend on various factors, such as grain size, grain boundaries, domain walls, stoichiometry, defect chemistry and porosity.

(ii) Effect of ceramic loadings and binder concentration

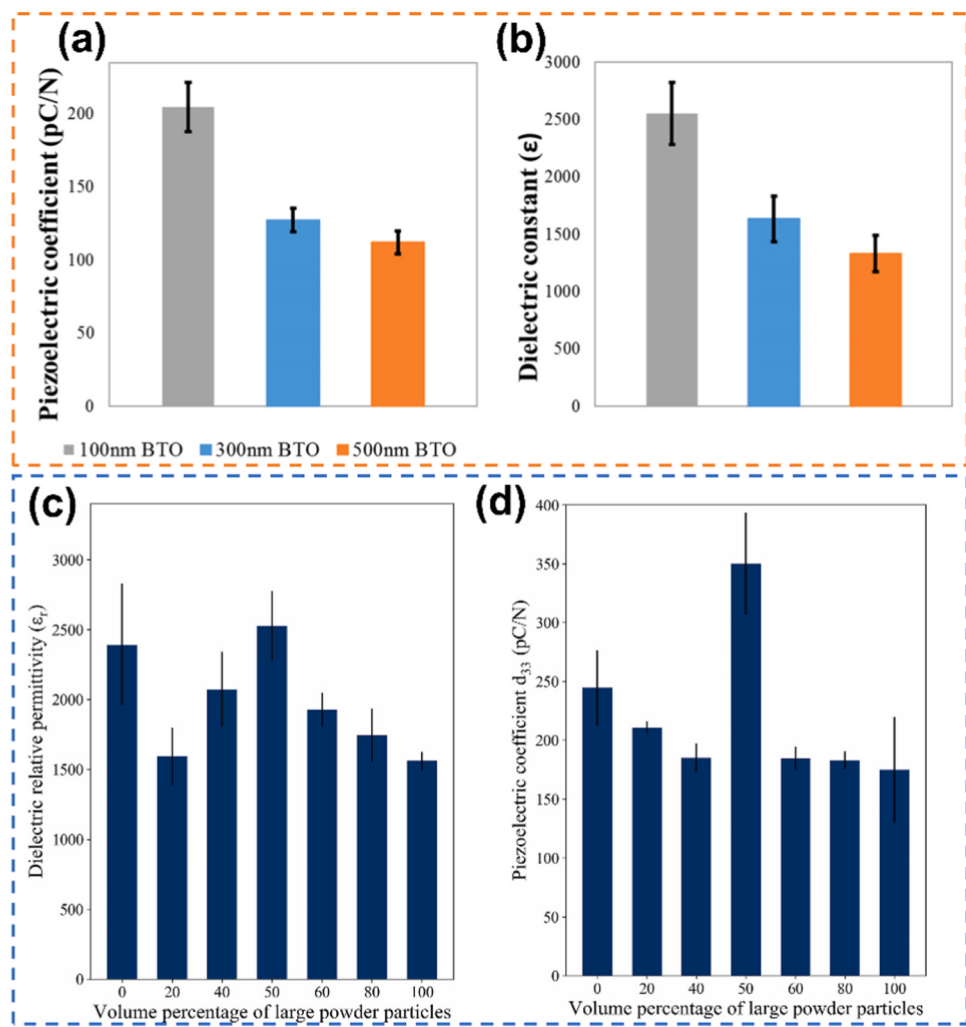


Fig. 35. Effect of particle size on the piezoelectric/dielectric properties. Variation of: (a) Piezoelectric coefficient, and (b) Dielectric constant as function of different unimodal particle size [58]. (c) Dielectric permittivity, and (d) Piezoelectric coefficient as a function of bimodal particle size, with different ratios of fine and coarse particles [61].

Reproduced from Ref.: (a-b) [58], with permission from IOP Publishing. (c-d) [61], with permission from Elsevier.

The electrical properties of functional ceramics are strongly influenced by the ceramic loading in the ink. As the ceramic loading increases, the amount of binder decreases, leading to improved densification and reduced porosity. Lorenz *et al.* reported that the dielectric and piezoelectric response of the sintered ceramic increased on increasing ceramic loading from 50 to 52 vol%. The samples fabricated with 52 vol% exhibited higher piezoelectric coefficient and relative permittivity values, as illustrated in Fig. 36(a-b) [69]. However, this improvement works just up to a certain threshold. For instance, Cheng *et al.* used different amounts of BT (70 wt%, 75 wt%, 80 wt%, 82 wt%, 84 wt%, 86 wt%) and found that the piezoelectric (96–133 pC/N) and ferroelectric response increases to 80 wt% of ceramic loading, but slightly decreased beyond this point as evidenced by the P/E hystereses in Fig. 36(c) [194]. A similar variation in the properties has been reported by several authors [127,137]. In general, the polarization value also increases with the applied electric field as shown in Fig. 36(d), since the polarization is proportional to the electric field.

It has been reported that beyond an optimal point, further increase in ceramic loading can lead to higher viscosity, resulting in processing difficulties and defects that can negatively impact the properties [61, 114,121,145]. Therefore, maintaining an optimal balance between ceramic loading and binder content is crucial for achieving superior electromechanical performance.

In a recent study, authors explicitly reported the effect of different amount of binder on the electrical properties. For this, the binder concentration was varied from 6–12 wt% (in steps of 2 wt%). It was found that with 10 wt% binder, the grain growth was optimal, the particle size was uniform, and there were fewer defects, leading to a maximum in the dielectric and piezoelectric response (Fig. 36(e-f)) [84]. The authors also correlated this behaviour with the shape of the ferroelectric domains. For ceramics containing up to 6 wt% binder, the sintered ceramics exhibited a reversible 90° domain configuration. However, with higher binder concentrations, the grain size increased, leading to the appearance of irreversible 180° domain configurations. At a binder concentration of 12 wt%, the ceramics contained only irreversible domains. A similar effect has been reported for samples with different binder saturation (75 %, 90 %, and 120 %) values [162]. Maximum d_{33} value was reported for the sample fabricated with binder saturation of 90 % (Fig. 36(g)). The use of excessive binder might generate a local over-pressure on the powder bed, resulting in the movement of particles away from each other. This can potentially hinder densification during sintering, resulting in decreased piezoelectric properties.

(iii) Effect of sintering temperature, hold time and cooling rate

The sintering temperature and holding time significantly impact the

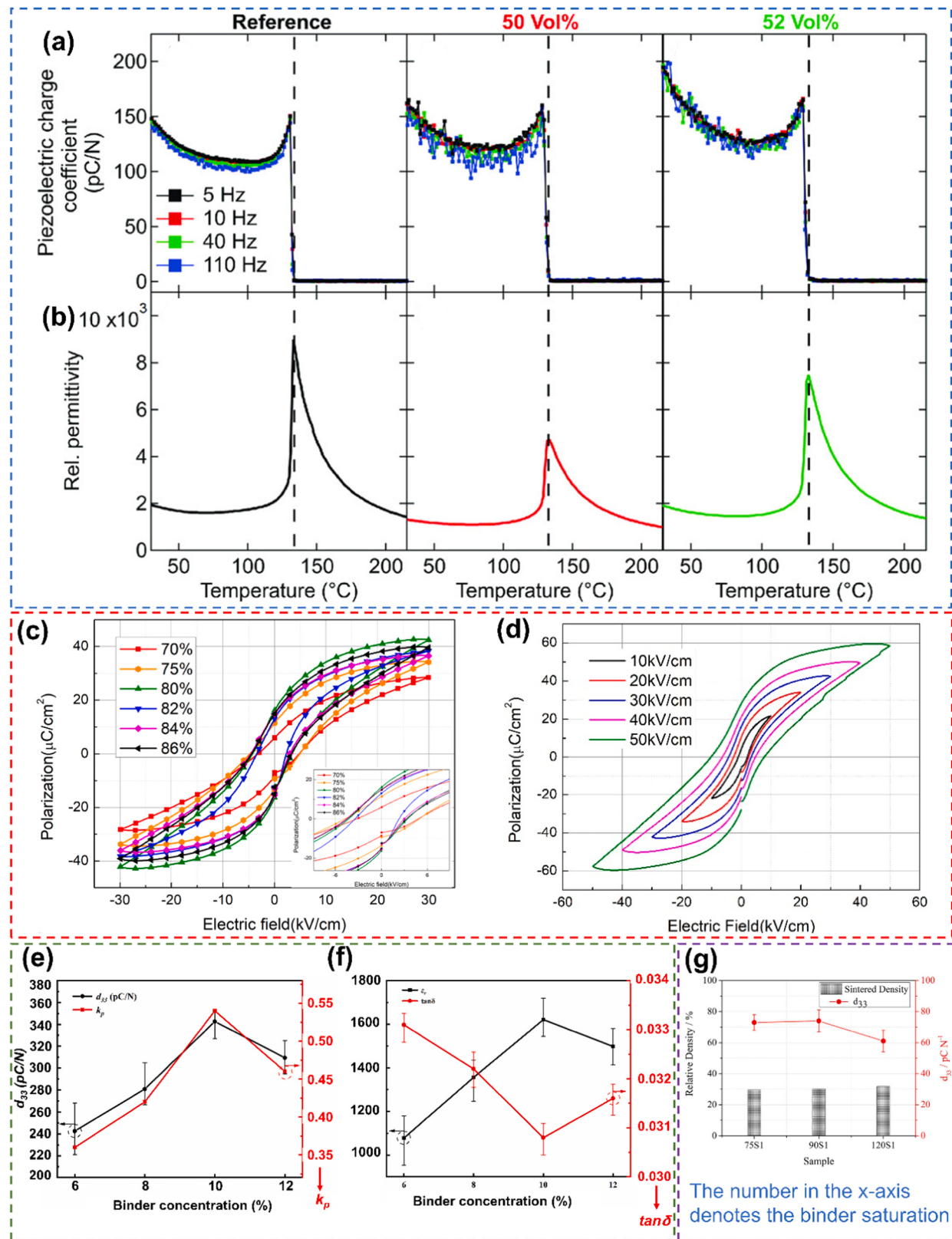


Fig. 36. Effect of the ceramic loading and binder concentration on the electrical properties. (a) Piezoelectric charge coefficient, and (b) Relative permittivity as a function of temperature for BT samples fabricated with varying amount of ceramic loadings [70]. (c) Polarization-electric field (P-E) hysteresis loops of sintered ceramics with different BT concentration (inset shows the magnified image highlighting the remanent polarization). The corresponding P/E loops for 80 wt% BT with different electric fields are shown in (d) [224]. The effect of the binder (PVA) content on the (e) Permittivity and dielectric loss, and (f) Piezoelectric coefficient of PZT ceramics [85]. (g) Variation of the piezoelectric coefficient as a function of the binder saturation value for binder jetted KNN samples [191]. (a-b) [70], (c) [224], Open access article distributed under the terms of the Creative Commons CC BY license. Reproduced from Ref.: (d-e) [85], and (f) [191], with permission from Elsevier.

microstructural and electromechanical properties. As the sintering temperature increases, the mechanisms of mass diffusion in the material are enhanced. The phenomena of densification and grain growth occur more rapidly. If the parameters are adjusted to obtain a dense microstructure, with desirable grain sizes, no defects and no porosity, this will result in a better dielectric and piezoelectric response from the material (Fig. 37(a-c)) [51,86,149]. Higher temperatures and appropriate holding times facilitate better sinterability, leading to larger, more uniform grains and reduced porosity, which enhance domain wall mobility and overall material response. However, beyond an optimal sintering temperature and holding time, properties begin to decline (Fig. 37(a-c)) [149,183,198]. This decline is attributed to over-sintering, which causes excessive grain growth, grain coarsening and the potential formation of secondary phases that disrupt the uniformity and stability of the material. Excessive grain growth can lead to decreased density and create undesirable internal stresses, ultimately reducing the dielectric and piezoelectric properties. Thus, while increasing the sintering temperature and optimizing holding time initially enhances the properties by improving microstructural characteristics, surpassing the optimal point results in a degradation of these properties due to the adverse effects of over-sintering. Moreover, to avoid the large grain size that could reduce the piezoelectric properties, a recent study with 3D printed BT used a step cooling profile, resulting in an average grain size around 1 μm with d_{33} value reaching 420 pC/N (Fig. 37(d)) [93]. However, the d_{33} value increased from 290 to 360 pC/N on increasing the dwelling time from 2 to 20 h resulting in a grain size up to 2 – 3 μm , which is less than the value obtained using the step cooling process (see Fig. 29(g-i) for the microstructure).

(iv) Effect of texturing

Texturing has a significant impact on the properties of piezoelectric ceramics by aligning the grains in a preferred crystallographic orientation. This alignment significantly increases the piezoelectric coefficients of ceramics.

For instance, Zheng *et al.* reported that in PMN-PT ceramics, textured via BT platelets, d_{33} was approximately 60 % higher compared to non-textured ceramics [162]. Additionally, texturing affects other properties as well. The remanent polarization (P_r) decreases from 25.5 $\mu\text{C}/\text{cm}^2$ for non-textured samples to 19.5 $\mu\text{C}/\text{cm}^2$ for textured samples (Fig. 38 (a)). The maximum ε_r at T_c decreases from approximately 22,100 in non-textured ceramics to around 18,500 in textured ceramics (Fig. 38 (b)). This decrease in ε_r in textured ceramics is primarily associated with the lower dielectric ε_r of BT platelets at T_c compared to the matrix. However, at room temperature, the ε_r is higher for the textured samples which can be related to the enhanced extrinsic contributions at low temperatures (Fig. 38(b)). Extrinsic contributions such as domain reorientations play a more significant role at lower temperatures, when the unit cell distortion is larger. Furthermore, the maximum unipolar strain (S_{\max}) at 25 kV/cm is 0.20 %, which is about 1.4 times that of the non-textured sample (Fig. 38(c)). Similar results were reported by Walton *et al.*, who observed a substantial improvement in strain and piezoelectric coefficient values that became more pronounced with increasing aspect ratio of the extrusion nozzle [91]. This significant enhancement in strain is another proof to the improved performance of textured ceramics.

Similarly, Du *et al.* reported a larger piezoelectric coefficient ($d_{33} = 275$ pC/N) in printed textured BT ceramics compared to non-textured BT ceramics ($d_{33} = 172$ pC/N) [163]. This improvement in the piezoelectric properties is accompanied by a significant enhancement in remanent polarization (P_r) values, with non-textured and textured samples showing approximately 6.15 $\mu\text{C}/\text{cm}^2$ and 14.88 $\mu\text{C}/\text{cm}^2$, respectively

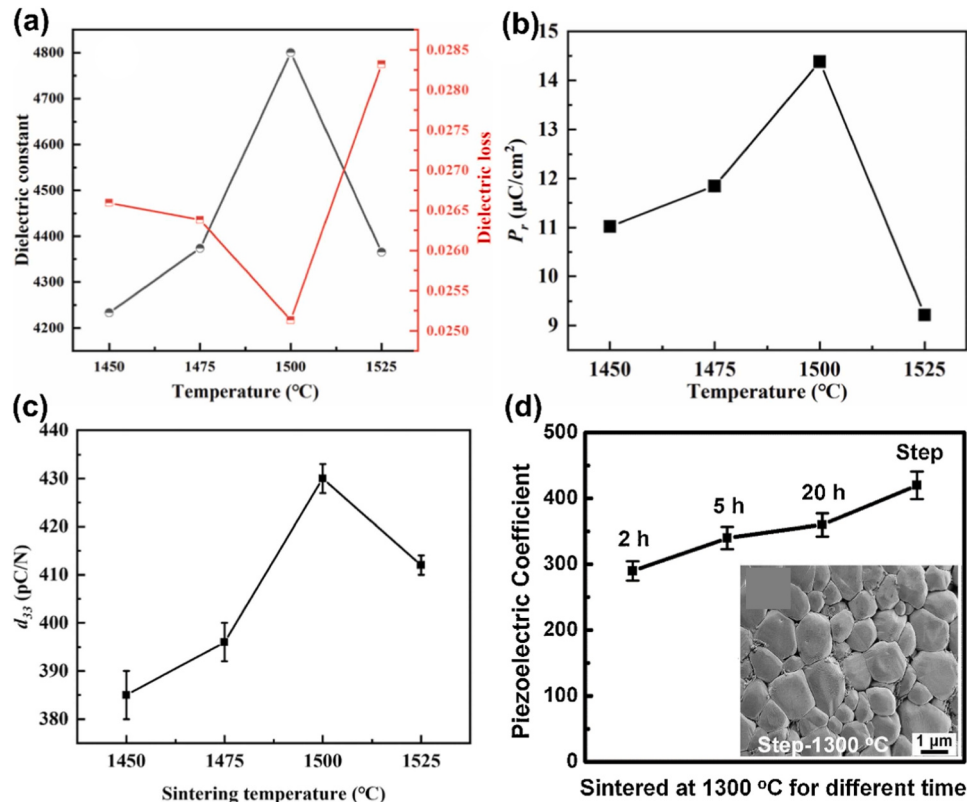


Fig. 37. Effect of the sintering temperature, hold time or cooling time on the electrical properties. Variation of the (a) Permittivity and dielectric loss, (b) Remanent polarization, and (c) d_{33} as a function of sintering temperature for sintered BCZT ceramics [149]. (d) Impact of dwelling time and step cooling process on the piezoelectric coefficient of sintered BT ceramics [93]. The inset shows the micrograph for the step cooled sample.

Reproduced from Ref.: (a-b) [149], and (c-d) [93], with permission from Elsevier.

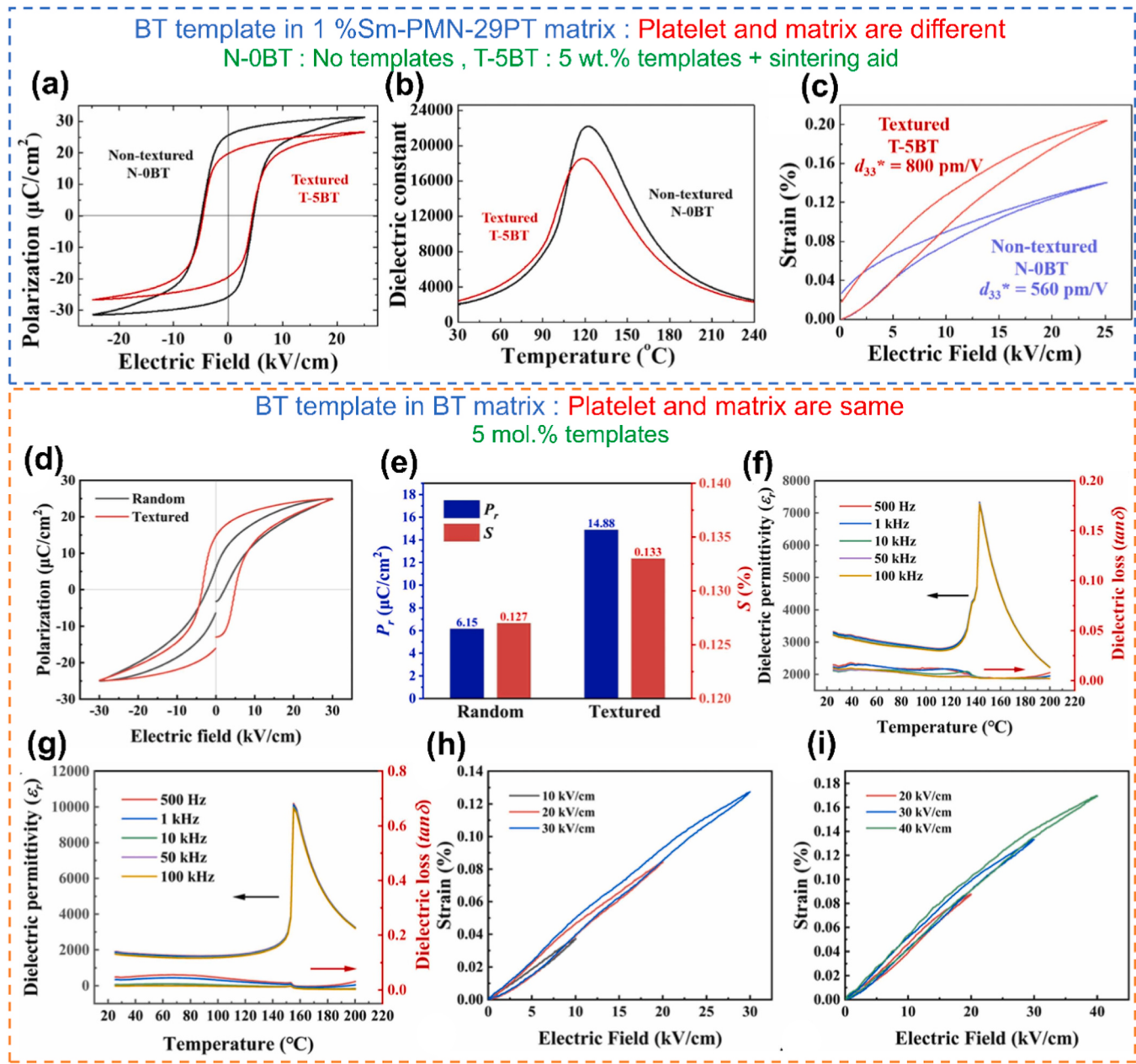


Fig. 38. Texturing effect on different electrical properties. Effect of texturing on [162]: (a) Polarization-electric field (P-E) hysteresis loops, (b) Temperature dependent permittivity at 1 kHz, and (c) The unipolar strain by using BT platelets in a PMN-PT matrix. Effect of texturing using BT platelets in a BT matrix [163]: (d) Polarization-electric field (P-E) hysteresis loops, (e) Comparison of the remanent polarization and strain at an electric field of 30 kV/cm, and Dielectric permittivity, dielectric loss, and strain of (f, h) Random, and (g, i) Textured BT ceramics sintered at 1300 °C.

Reproduced from Ref.: (a-c) [162], and (d-i) [163], with permission from Elsevier.

(Fig. 38(d-e)). The enhanced P_r is attributed to the more effective alignment of dipoles in the $<001>$ -textured BT ceramics under a high direct current electric field. Furthermore, at 1 kHz and 25 °C, the textured samples exhibit a smaller permittivity (~1867) compared to the random samples (3303) (Fig. 38(f-g)). The dielectric loss increases in the textured sample. When subjected to an electric field of 40 kV/cm, the strain value exhibits a maximum of 0.17 % for the textured one (Fig. 38(i)). In contrast, the random oriented samples are broken with such high field (Fig. 38(h)). Buessen *et al.*, developed an internal stress model that correlates the permittivity and the 90° domain configurations [230]. At room temperature, a BT single crystals show strong anisotropy in the permittivity with highest values along the a axes [231,232]. In polycrystalline BT, the permittivity may reach even higher values due to complex domain configurations and phase transformations, which allow

more directions for the reorientation of the spontaneous polarization and stress distributions [16]. Using large plate-shaped particles to texture the material may have a positive effect on the piezoelectric constant. However, the permittivity might be reduced due to limited possibilities for the polarization orientations.

The reason for the larger piezoelectric coefficients is that texturing aligns the domains more uniformly towards the external loading direction. This alignment optimizes the contribution of each domain to the overall piezoelectric response, significantly increasing the piezoelectric coefficients. In addition to enhancing piezoelectric properties, texturing reduces grain boundary scattering and ensures a more uniform stress distribution across the material. The uniform domain alignment facilitates the material's ability to undergo larger deformations when an electric field is applied, resulting in high strain. Additionally, the

alignment enhances the material's ability to retain polarization after the removal of the external electric field, leading to a higher P_r . This not only improves the mechanical stability of the ceramics but also contributes to their overall performance and reliability in various applications.

(v) Effect of sintering additives or dopants

The main purpose of adding sintering additives or dopants is to enhance the functional properties. As discussed before, Copper oxide (CuO) is one of the most widely used sintering aid to improve the densification behaviour of the ceramics by forming a transient $\text{CuO}-\text{BaO}$ liquid phase and facilitating liquid-phase sintering [184]. The electrical properties of the CuO -doped ceramics increase up to a certain concentration because of the increase in the density and grain size (Fig. 39(a-c), please refer to Fig. 34(c-d) for the corresponding microstructures). The grain growth facilitates the movement of domain walls during the polarization process, while the increase in density leads to a more even distribution of electric fields and enhanced polarization efficiency. Further increasing the concentration, the porosity reappears in the samples (or the density decreases) that deteriorates the ferroelectric response.

In a recent study, authors have introduced Sn^{4+} to substitute Ti^{4+} at B-sites in BT ceramics [167]. With increasing Sn^{4+} content (up to 13 mol.%), the room temperature ϵ_r increases. This is due to fact that the ceramics with higher Sn^{4+} content (11, 13 mol.%) exhibited fine grains of about 1–5 μm . On the other hand, the grain sizes were in the order of

4–10 μm for Sn^{4+} content of 2 and 6 mol.%. The ferroelectric properties of such doped ceramics decrease with the increasing Sn^{4+} content, as evidenced by the thinning of the P-E loops (Fig. 40(c-d)). The P_r decreases significantly from 11.92 $\mu\text{C}/\text{cm}^2$ to 1.11 $\mu\text{C}/\text{cm}^2$. This can be attributed to the fact that since BaSnO_3 is non-ferroelectric, increasing the amount of Sn gradually changes the behaviour of a normal ferroelectric to a diffuse ferroelectric as depicted from the dielectric behaviour (Fig. 40(a-b)). The piezoelectric coefficient values increased up to 6 mol.% of Sn^{4+} because of bigger grains and enhanced density and thereafter decreased for higher concentration due to small grain size and reduced density as a result of insufficient sintering (as the Sn content increases, the sintering temperature increases correspondingly).

(vi) Effect of pore forming additives

The addition of pore-forming additives such as PMMA, PE, PS, SS, etc. has a detrimental effect on the piezoelectric and ferroelectric characteristics, as it results in the formation of residual porosity that remains even after the additives are removed during the subsequent debinding and sintering process [145,150,171–173].

With increasing amount of the PFAs, the ϵ_r and piezoelectric coefficient decreases because of the reduced sintered density (Fig. 41(a-b)) [150,171,172]. The ferroelectric behaviour exhibits a similar response (Fig. 41(c)). The presence of residual porosity after debinding results in an increase of the unpolarized region (pores) in the sintered ceramics (or in other words, decreasing the active area for polarization). The higher the amount of PFAs, the lower is the response. A similar effect is

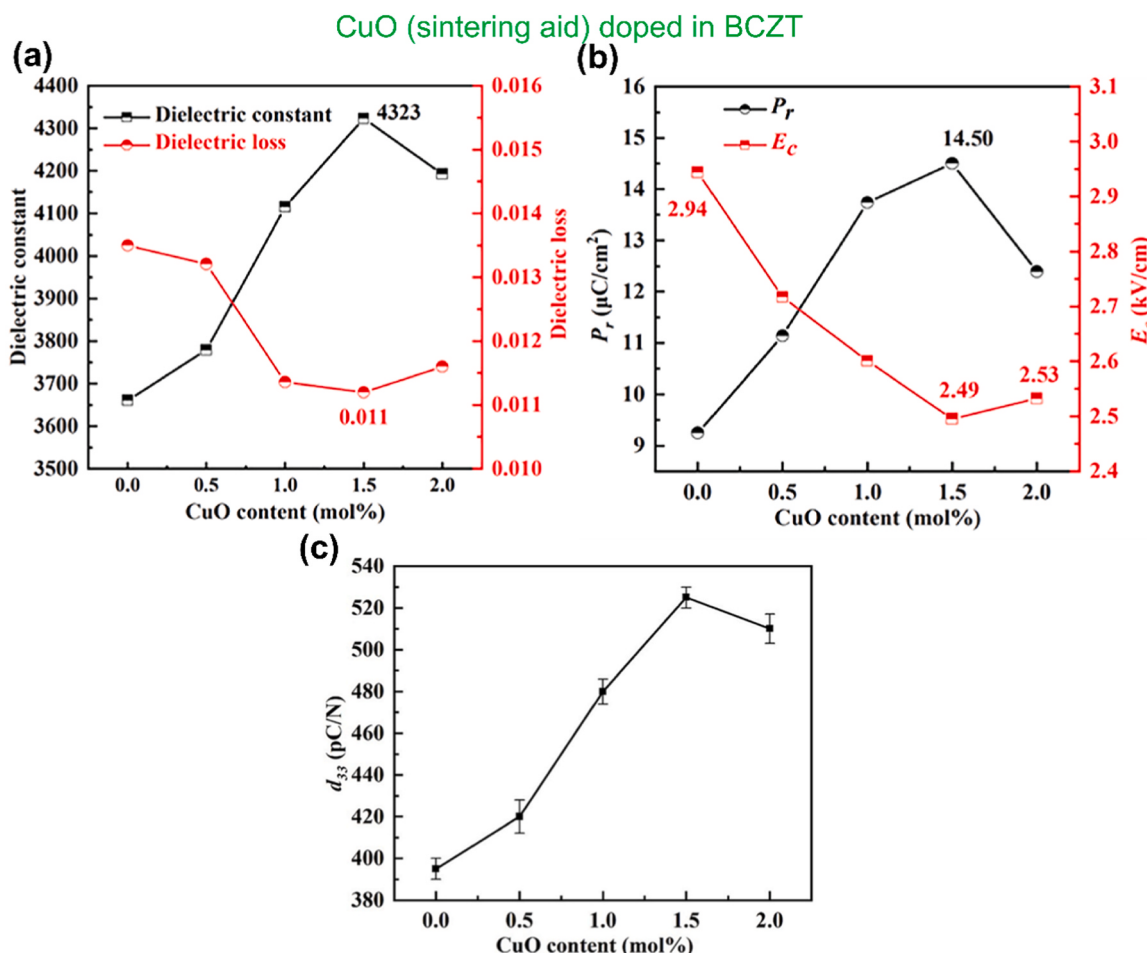


Fig. 39. Effect of sintering aid on the electrical properties. Variation of (a) Permittivity and dielectric loss, (b) Remanent polarization, and (c) Piezoelectric coefficient of BCZT ceramics doped with varying CuO content [184].
Reproduced from Ref.: (a-c) [184], with permission from Elsevier.

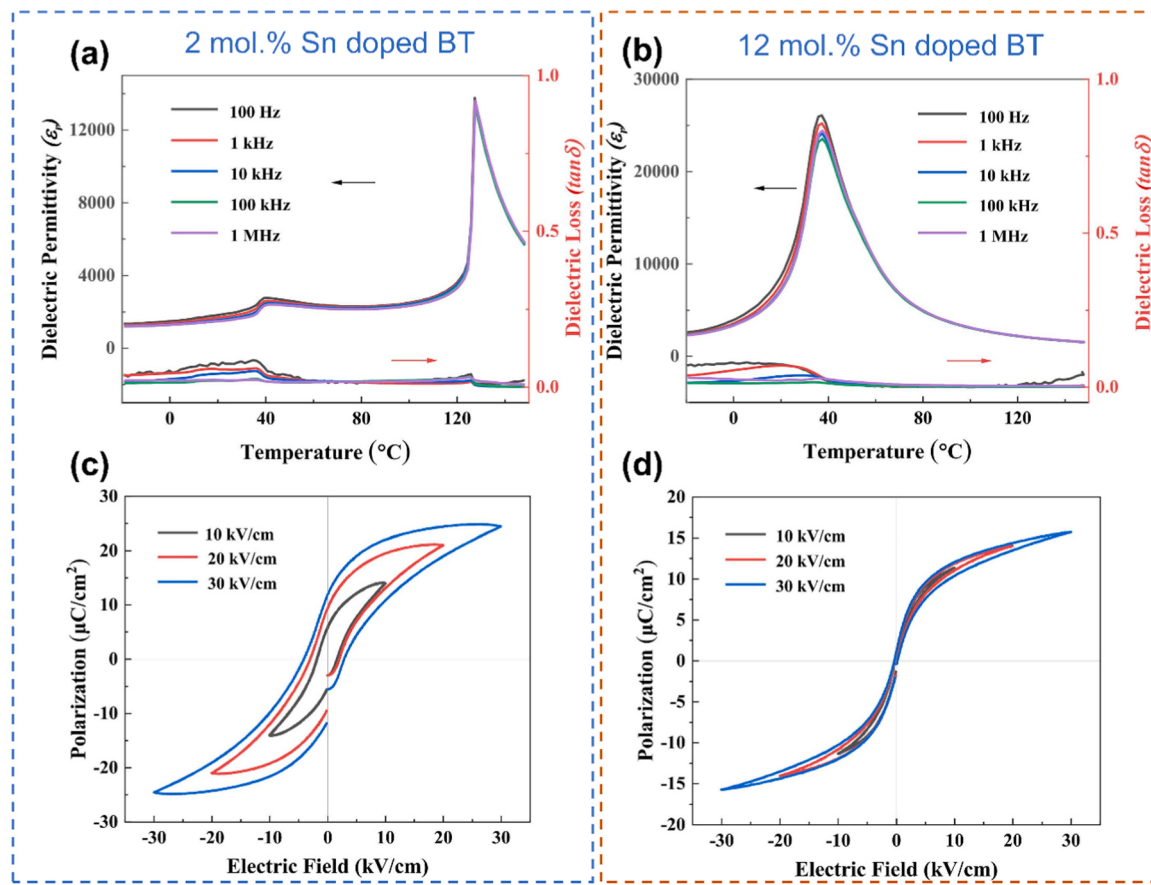


Fig. 40. (a-d) Variation of the dielectric and piezoelectric properties with varying Sn^{4+} content in BT ceramics [167]. Reproduced from Ref.: (a-d) [167], with permission from Elsevier.

observed on increasing the particle size of the PFAs [173].

(vii) Effect of the design

The design of the printed geometries has the potential to significantly alter the functional properties that may not be achieved with conventional shaped geometries. Several studies have reported the effect of the design or the infill density on the properties of the fabricated component.

Hierarchical porous PZT as depicted in Fig. 42(a), with different amounts of ceramic phase exhibit different overall porosities [98]. The ϵ_r values and the piezoelectric coefficients increase with the increasing the overall fraction of the ceramic phase that actively contributes to the functionality. As evidenced in Fig. 42(b-c), since the decrease/increase in d_{33} was more gradual when compared to ϵ_r , the g_{33} value decreased with increasing porosity. The authors reported by varying the geometrical porosity (along with the porosity developed due to freeze casting) they could achieve really high d_{33} , g_{33} and better sensitivity.

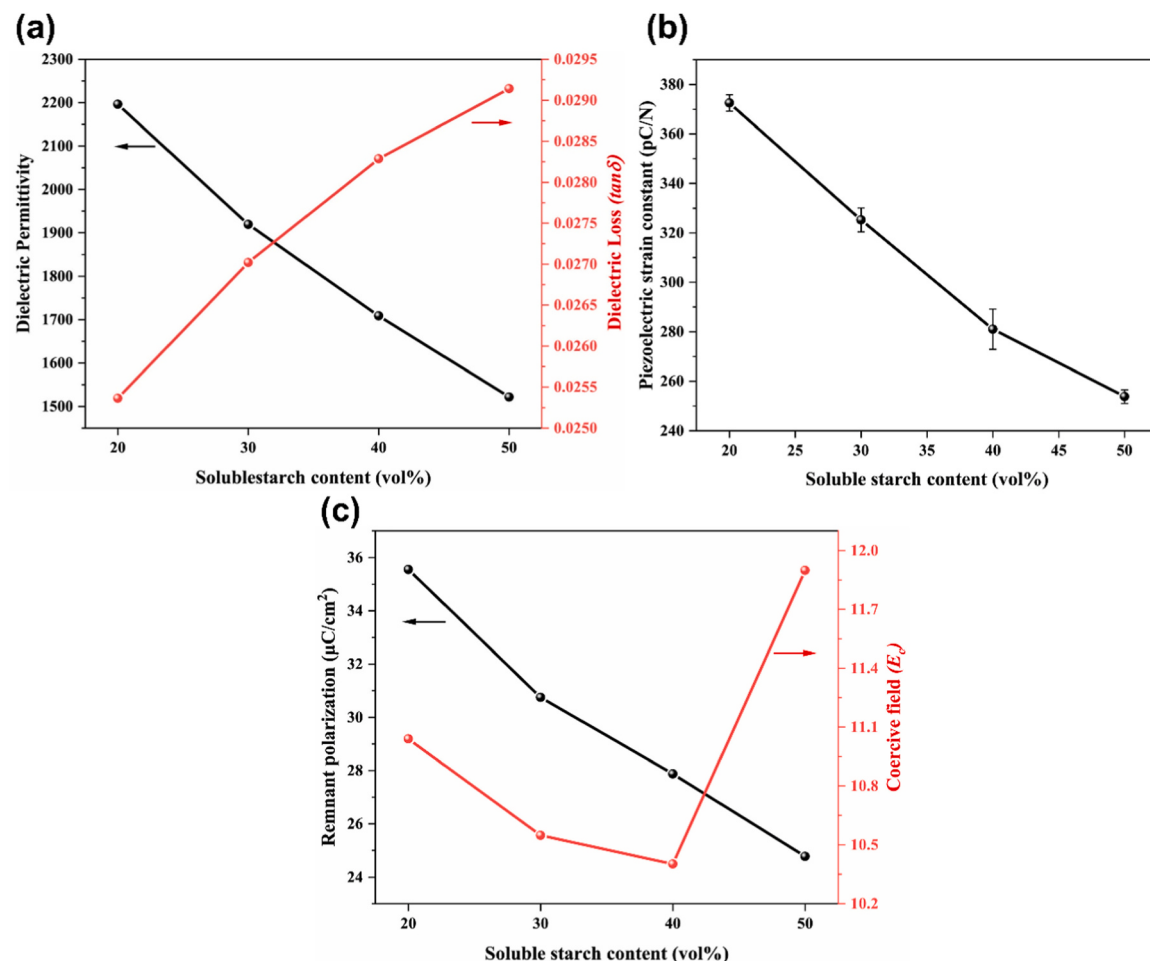
In another study, authors reported the effect of an open and offset scaffold structure on the electromechanical properties [116]. A significant decrease in the electromechanical properties was observed when comparing the scaffold and offset sample with the powder pressed pellet (Table 7 and Fig. 42(d)). In addition, the offset sample exhibited better properties than the open scaffold. Unlike in the open structure, where the pores are continuous and open, in an offset structure, these pores are closed when the next layer is printed (Fig. 42(e)). As a result, the effective polarizing material is higher in offset structures. The g_{33} is directly proportional to d_{33} and inversely proportional to the ϵ_r . One can clearly observe from Table 7, that the difference in the ϵ_r values is larger than the difference in d_{33} values. As a result when considering g_{33} value

for figure of merit (FOM), the open scaffolds outperform the offset structures.

A study by Ma *et al.* investigated the electromechanical properties of porous gyroid structures with varying designed porosities (55 vol% – 75 vol%) as shown in Fig. 42(f) [165]. The simulation results indicated that there was minimal difference in the electric field distribution between structures with 60 vol% and 70 vol% porosity. This finding suggests that the electric field distribution in porous structures is more dependent on the geometry of the structure rather than the level of porosity. Additionally, the study revealed that the piezoelectric coefficient d_{33} of the gyroid structure with 50 vol% porosity can approach values similar to those of bulk structures, though only under higher electric fields (Fig. 42(g)). This is due to the fact that porous ceramics require a stronger poling electric field to achieve complete polarization compared to their bulk counterparts. Notably, the d_{33} values remained stable even as porosity increased (Fig. 42(h)). However, the dielectric constant and the polarization showed a significant decrease with higher porosity. Such results prove that the d_{33} is independent of the amount of the porosity in the structure (Fig. 42(i)). The strain however did not exhibit a straightforward relationship but was in the range of 0.07 – 0.1 %.

A recent study exhibited that by increasing the wall thickness of the triply periodic minimal surface (TPMS) structures, the ϵ_r and d_{33} values increase [192]. Moreover, these TPMS structures exhibited better sensitivities and efficiencies when converting mechanical energy to electrical and vice versa. Such sensitivities and efficiencies were measured by comparing the electromechanical coupling coefficient.

(viii) Effect of properties along different direction

**Fig. 41.**

Effect of using different amounts of PFAs. (a) Variation of the: (a) Permittivity and dielectric loss, (b) Piezoelectric coefficient, and (c) Remanent polarization of sintered PZT ceramics with varying amount of soluble starch [150]. Reproduced from Ref.: (a-c) [150], with permission from Elsevier.

The dielectric and piezoelectric properties of the sintered samples vary depending on the poling directions or the direction in which they are tested. Ceramics fabricated using BJ technology exhibit high orthotropy due to voids formed during both the fabrication and heat treatment processes. These voids significantly impact several properties of the printed ceramics, especially their functional properties.

Recent findings indicate that the piezoelectric properties of binder jetted BT depend on the testing orientation [200]. Samples tested perpendicular to the printing layers showed a piezoelectric response more than 35 % higher than those tested parallel to the layers. Additionally, the dielectric properties were 20 % better in the samples tested perpendicularly, compared to those tested in parallel. A similar result was reported for PZT samples fabricated by BJT, showing higher piezoelectric properties for samples tested perpendicularly, compared to those tested parallelly [193]. The average piezoelectric response for the parallel samples was 468.5 pC/N, while the perpendicular samples yielded 541.4 pC/N (Fig. 43(a)). In another study on BJ-printed KNN, the d_{33} was measured both parallel and perpendicular to the layer deposition direction [191]. However, the effect of the testing orientation appeared to be minimal. The d_{33} value in the parallel orientation was approximately 84.8 ± 9.2 pC/N, while in the perpendicular orientation it was 89.9 ± 3.8 pC/N.

The differences in dielectric and piezoelectric properties of ceramics in different orientations arise from the anisotropic nature of the binder jetting additive manufacturing process. In the perpendicular orientation, the layer-by-layer fabrication results in a microstructure with

oriented porosity that forms a set of capacitors arranged in a parallel circuit (Fig. 43(b)). Consequently, there is no negative impact on the electrical performance. However, in the parallel direction, the porosity forms a series circuit, which lowers the electrical properties of the system (Fig. 43(c)) [200]. In contrast, BJ-printed KNN shows minimal directional differences due to higher densities and uniform internal porosities, maintaining consistent structural integrity despite some preferential porosity orientation [191].

The phenomenon of anisotropy has been also reported for samples fabricated with DIW (Fig. 43(d)) [70]. The anisotropy was more pronounced in samples with lower ceramic loadings (50 vol%) due to their low relative densities after sintering. However, no significant differences were noted in samples with 52 vol% ceramic loading, as they exhibited better densification and limited residual porosity. Similar results were observed for samples fabricated using vat photopolymerization [190]. As the solid loading in the ink increased, the properties of the samples became almost identical in both directions as shown in Fig. 43(e).

Having examined the key parameters that influence piezoelectric and ferroelectric properties, it is essential to now assess the impact of the additive manufacturing process on these properties. When evaluating piezoelectric and ferroelectric characteristics in additive manufacturing (AM), it is critical to consider not only the printing and sintering parameters, but also the properties of the initial powder input. Even minor differences in powder characteristics such as particle size distribution, surface chemistry, purity, and morphology can have a major impact on sintering behaviour and ultimately, material properties. Because of

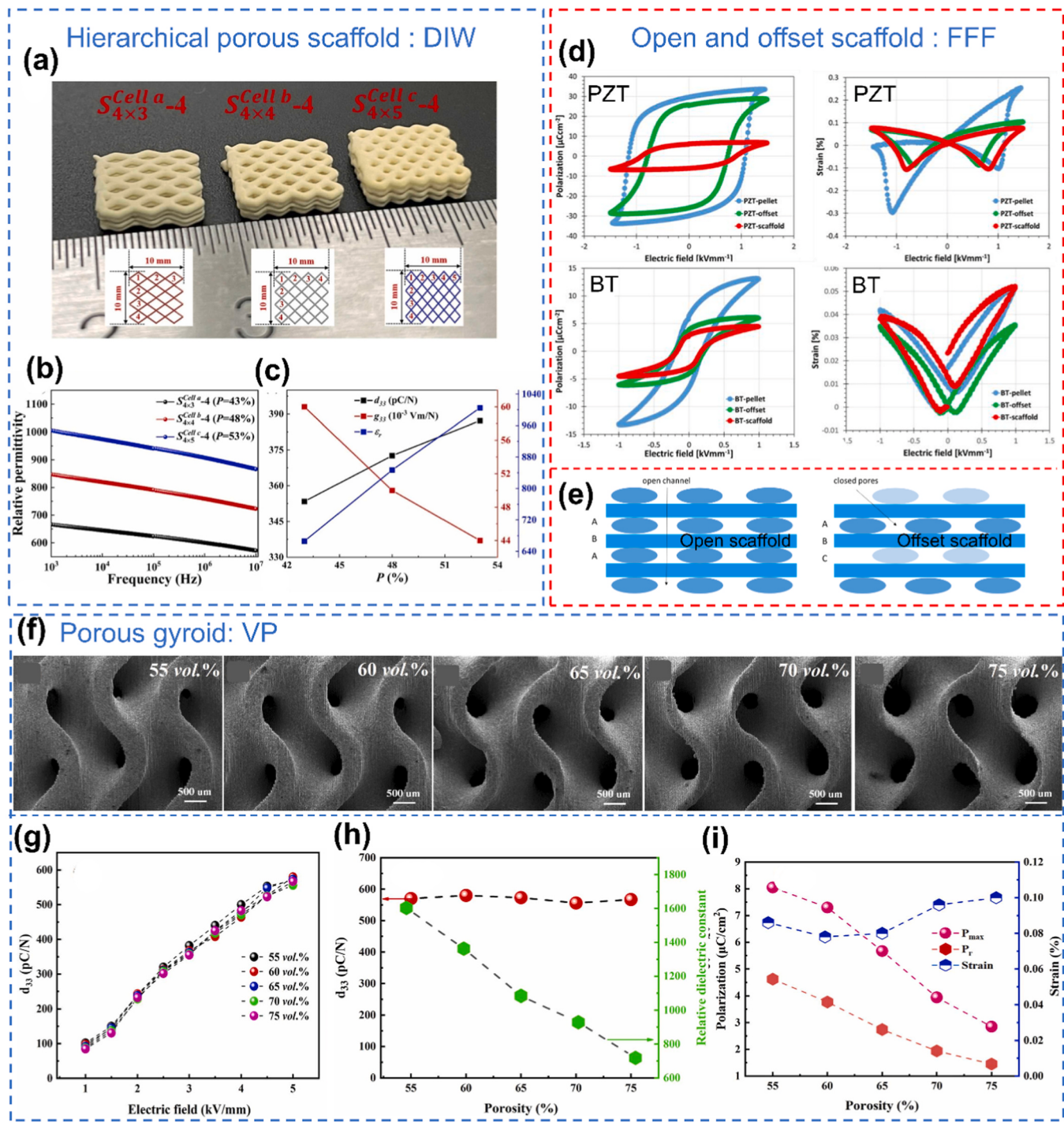


Fig. 42. Design dependent electrical properties. (a) Optical image of the hierarchical porous PZT scaffolds with different infill density. The corresponding evolution of permittivity as a function of frequency, piezoelectric coefficient, d_{33} and piezoelectric voltage coefficient, g_{33} has been shown in (b-c) [98]. A comparison of electromechanical properties between powder pressed and 3D printed samples for (d) PZT and BT ceramics. The schematics of two different 3D-printed geometries are schematically shown in (e) [116]. (f) Overview SEM images of the sintered BCZT gyroids with different volume of porosities and their corresponding variation in d_{33} , dielectric constant, polarisation, and strain are shown in (g-i) [165]. Reproduced from Ref.: (a-c) [98], and (f-i) [165], with permission from Elsevier. (d-e) [116], Open access article distributed under the terms of the Creative Commons CC BY license.

these variations, when comparing additive manufacturing processes, it is challenging to distinguish between the effects of the manufacturing process and those of the feedstock. However, we have tried our best to highlight meaningful differences that may arise specifically due to the additive manufacturing process employed. The property gaps observed between piezoelectric ceramics fabricated using different AM methods can be attributed to several key factors, including the particle size of the

feedstock, binder content, sintering efficiency, microstructural homogeneity, and anisotropy.

The differences in properties between various AM techniques can be largely attributed to variations in density. For instance, one can clearly notice in Table 11 that the properties of binder-jetted samples are noticeably inferior when compared to those achieved by samples fabricated using DIW or VP. As a stringent requirement for the binder

Table 7

Comparison between pressed pellet and 3D printed open and offset scaffold structures [116]. (Open access article distributed under the terms of the Creative Commons CC BY license.).

	PZT (1.5 kV/mm)			BT (1 kV/mm)		
	Pellet	Scaffold	Offset	Pellet	Scaffold	Offset
$d_{33}(\text{pm/V})$	384	202	273	142	107	127
ϵ_r	1405	297	1177	3657	906	1372
$S (\%)$	0.36	0.19	0.18	0.04	0.04	0.04
$P_r (\mu\text{C}/\text{cm}^2)$	29.7	6.2	25.5	6.2	2.9	3.5
$g_{33} (\text{mVm/N})$	31	77	26	4	13	10
$FOM (d_{33} \times g_{33})$ (fm ² /N)	11904	15554	7098	568	1391	1270

jetting (BJ) process, the powders must be flowable. To achieve this, the initial feedstock often consists of relatively large particle agglomerates, sometimes in the order of 100 μm , which are usually granulates. The powder packing density cannot be very high in the BJ process and the granulates have to be densified during the sintering process. This limits the ability to achieve a densely sintered ceramic.

A similar conclusion regarding the properties can also be drawn for samples fabricated using SLS, as, like BJ, the properties of SLS-processed

samples are not particularly favourable. While the density values in Table 6 suggest that these samples are highly densified, the microstructure remains highly inhomogeneous, with numerous defects introduced due to the high-intensity laser used during fabrication, which might lead to inhomogeneous temperature distributions.

The arrangement of porosity in porous samples can give rise to directional properties. This effect is most noticeable in samples fabricated using binder jetting. In contrast, due to the high density achieved in extrusion-based methods and vat photopolymerization, no such anisotropy is observed in the sintered samples. This effect has also been observed in samples fabricated using VP and DIW at lower densities. As the density increases, the differences in properties along different directions diminish, eventually becoming almost identical.

The density achieved in vat photopolymerization (VP) is typically over 95 % in most cases, which can be attributed to the very fine particle size used as feedstock (Tables 4, 10). In contrast, extrusion-based techniques require a feedstock with particle sizes around 1 μm (Tables 2–3), where the driving force for sintering is lower (when compared to fine powders used in VP). Despite the binder content being comparable to that of FFF or even higher than that in DIW, the piezoelectric and dielectric properties remain quite impressive.

In summary, the ability to achieve high density and uniform

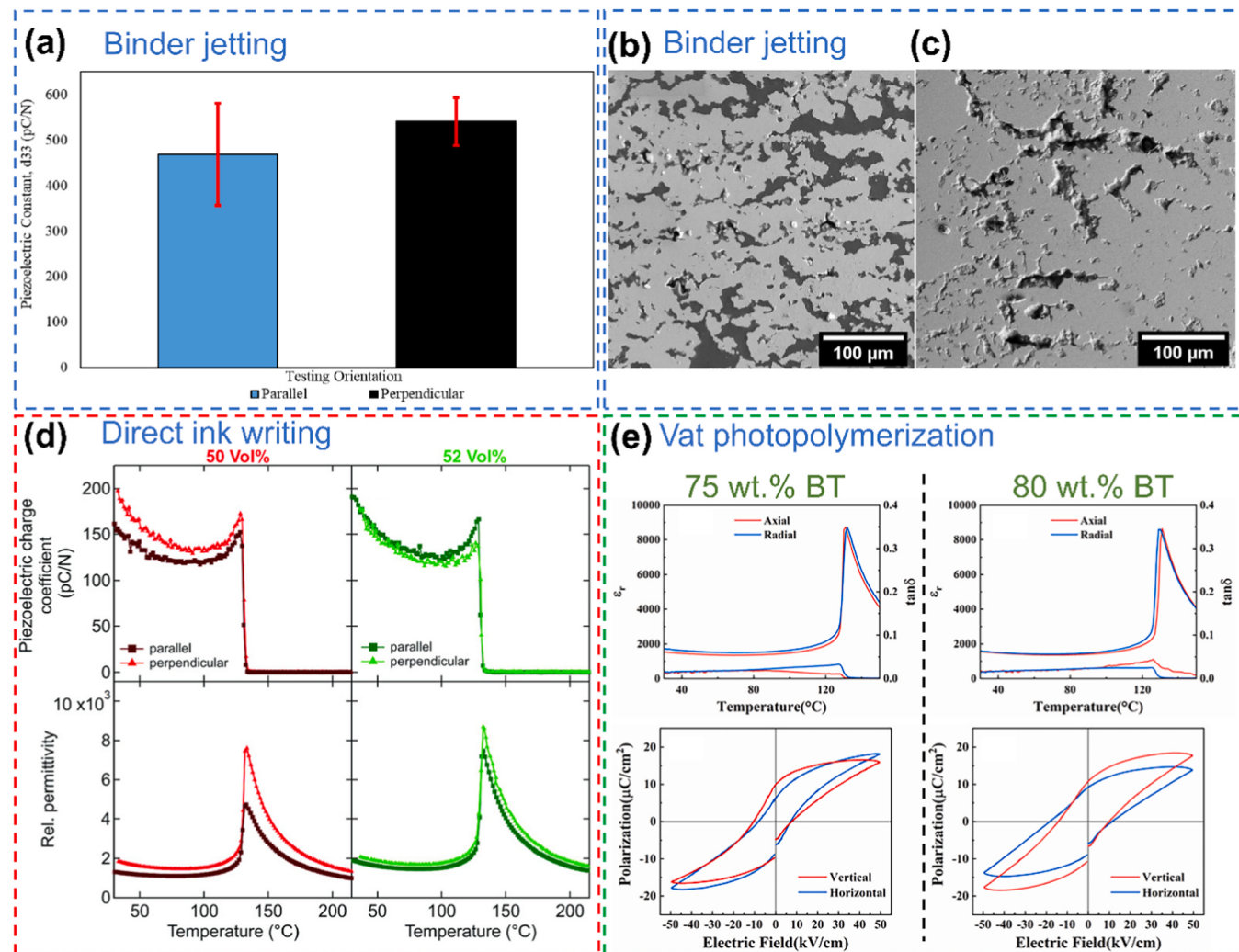


Fig. 43. Directional dependent electrical properties. (a) Piezoelectric coefficient as a function of the testing orientation for sintered PZT ceramics [193]. SEM images of the polished (b) Cross-section perpendicular to the printing direction, and (c) Surface parallel to the printing direction [191]. (d-e) Effect of the ceramic loadings and the measurement direction on the piezoelectric and dielectric behaviour of sintered BT ceramics [70,190].

(a) [193], (d) [70], Open access article distributed under the terms of the Creative Commons CC BY license. Reproduced from Ref.: (b-c) [191], and (e) [70,190], with permission from Elsevier.

microstructure plays a key role in the improved piezoelectric response. Techniques such as DIW and VP provide more homogenous microstructures, greater densities, and enhanced piezoelectric characteristics, while BJ and SLS are more susceptible to inhomogeneous microstructure and flaws that compromise performance. Each AM approach has unique benefits and limitations, and knowing these underlying elements is critical for improving piezoelectric ceramic performance in additive manufacturing. It is important to note that, at this stage, it is challenging to draw definitive conclusions about FFF due to the limited number of studies that deal with sintering and functional characterization of the fabricated components.

If achieving high dielectric and piezoelectric properties is the goal, one should opt for DIW or VP. With VP, there is more design flexibility compared to DIW. However, it is not possible to draw definitive conclusions based solely on the values reported in Tables 8 – 11. A technically sound comparison can only be made if the starting powder and ceramic loading are identical for all AM processes, as even slight deviations can significantly affect the properties. For instance, the initial ceramic loading determines the green density: the higher the green density, the better the densification, and consequently, the better the final properties.

4. Benefits of using AM over powder pressed samples

The preceding sections of this article have been devoted to the analysis of the systematic impact of various parameters on feedstock development and post-processing conditions. However, it is important to point out clearly the distinct advantages that AM offers over conventional manufacturing processes for piezoceramic components.

Commercial piezoelectric devices are often in the form of simple shapes like disks, plates, rods, rings, tubes, cylinders and plates (Fig. 44) [233,234]. These devices are mostly fabricated by using hydraulic presses with desired press molds [234]. In the case of producing devices containing different materials, tape-casting is followed by machining methods to produce the desired geometry [235]. Such machining methods are rather complex and limit the processing possibilities for fabricating complex geometries. Furthermore, the substantial volume of waste produced during the machining process necessitates cautious handling when it comes to recycling or disposal, especially when lead-based formulations are used. In contrast, AM technologies, owing to their layer-by-layer approach, enhance the process efficiency by minimizing the waste generated. This is a step towards a more sustainable manufacturing process. In addition to the flexibility in the designs offered by the AM technologies, the additional benefit of addressing environmental sustainability is worth mentioning.

Material extrusion-based AM techniques have been extensively utilised and harnessed for the production of lattice structures [49–51,54, 56,71,83,85,88,92,94–98,104,116,131,133] (Fig. 45). These structures are defined by their repetitive and interconnected framework of extruded struts giving rise to a porous structure (designed porosity) as shown in Fig. 45(a-b), providing numerous benefits in diverse applications. In bone-tissue engineering applications, where piezoceramics can assist with regeneration by providing electrical charges in the bone, which in turn promote growth and repair. In this context, interconnected geometrical porosity is of crucial importance for efficient transportation of the essential nutrients, waste products and migration of the cells for the growth as well as other vital processes (Fig. 45(a-b)) [96,97]. The design of lattice structures can be precisely modified by employing various infill geometries and porosities (Fig. 45(a-h)). For instance, different infill geometries can alter the heating behaviour and heat transfer rate when used as a ceramic heater (Fig. 45(g-h)). [71]. In addition, it can also affect the piezoelectric and dielectric response [98]. Jia *et al.* reported that periodically porous structures exhibited better performance in pulsed-power energy conversion applications when compared to their bulk counterpart [94], thanks to the AM technologies that allow for the fabrication of structures with controlled porosity. In

addition, it is also possible to design structures with graded porosity, thus enabling to tailor desired properties to meet specific requirements. The fabrication of a Fresnel zone plate lens (FZPL) serves as great evidence of a graded structure (Fig. 45(i)) [107]. In general, the lattice structures are lightweight and with specialized infill geometry such as a gyroid, a structure with high strength-to-weight ratio can also be obtained.

AM can be used for fabricating geometries with various degrees of connectivity between the active ceramic phase or the passive phase (in this case, the porosity), out of which the 3–0, 3–3 and 2–2 architectures are quite difficult to produce with conventional techniques. Here, the first number refers to the connectivity of the ceramic phase and the second number refers to the connectivity of the geometrical porosity [237]. The electromechanical properties are dictated by the distribution of the two different phases. Specifically, components fabricated with 3–3 connectivity are reported to exhibit enhanced figures of merit (FOM) or improved piezoelectric energy harvesting properties [88,116,133]. In particular, the 2–2 connectivity has been widely used in the reported literature for transducer applications as well (Fig. 45(j)) [99,122]. Moreover, complex architectures have also been successfully fabricated using DIW, where the ink rheology is crucial for the shape retention (Fig. 45(k)) [93].

One prominent and appealing characteristic of extrusion-based techniques is the ability to fabricate structures using multiple materials (depending on the number of nozzles the printer has), thus enabling an extensive array of functionalities and applications. For instance, BT and Ni-BT multilayer structures were successfully printed and sintered under controlled atmosphere conditions to mimic a structure similar to a multilayer capacitor (Fig. 46(a)) [92]. In another study, a multi-layered transducer component was fabricated by depositing hard and soft PZT alternatively in a layer-by-layer fashion [103]. Such multi-material multilayered structures are reported to offer potential benefits in terms of performance, transmittivity and sensitivity. Tube actuators with PMN-PT and silver-palladium electrodes were also developed as a proof-of-concept for enhancing the displacement properties along the tube (Fig. 46(b)) [238].

Some more recent advancements demonstrate that it is possible to fabricate complex twisted spiral structures, in spite of the inherent brittle nature of ceramics (Fig. 47(a-b)) [72]. These structures exhibit a unique macro structure that was previously challenging to fabricate. Modern innovations have led to the creation of even more complex kirigami-origami constructions, which combine the delicate techniques of origami paper folding with the precise principles of Japanese paper cutting (Fig. 47(c-e)) [69]. Such structures can be potentially used in wearable electronics and health monitoring devices. Another example of advancement is the fabrication of free-standing pillars, which can potentially be used for drug delivery, cell cultivation, light emitting diodes, etc. (Fig. 47(f)) [84].

With extrusion-based AM techniques, it is indeed possible to fabricate large components (at least of the order of even a few centimetres). However, the resolution of such printed components is limited by the nozzle size of the extruder, which is typically greater than 400 μm (Tables 2 – 3), with the smallest nozzle size being reported as fine as in the order of 100 – 150 μm [49,88]. In addition, printing structures with large overhangs cannot be printed without support structures, making the post-processing challenging. The samples fabricated using such techniques, often exhibit a rough surface finish, that can be further processed using machining, for samples fabricated with FFF technology. On the contrary, such machining steps cannot typically be carried out on structures fabricated using DIW, as the printed structures are delicate and cannot handle such rough post-processing conditions. It is important to highlight that FFF overperforms DIW in cases where the nozzle has to move repeatedly over the deposited layer. For instance, in order to fabricate small hollow cylinders for transducer applications, FFF is always a better choice as the deposited struts are solidified immediately (and the presence of a cooling fan even makes it faster). This is valid as

Table 8

Post-processing conditionings and functional properties of samples fabricated with Direct ink writing.

Feedstock	Debinding conditions	Sintering conditions	Density (%)	Dielectric constant, ϵ_r	Dielectric loss, tan δ	Piezoelectric coefficient, d_{33} (pC/N)	Polarization, P_r ($\mu\text{C}/\text{cm}^2$)	Printed structure	Reference
Hard PZT	0.3 °C/min 600 °C 2 h	5 °C/min 1100 – 1300 °C 2h	~ 93.2 – 97.5			~ 268 ± 10		Ring shape	[74]
Barium acetate, TTIP		Argon: 3 °C/min 1200 – 1500 °C 2 h	97.8	533				Honey comb, Lattice, Dense cube	[78]
BaTiO₃ Hydrothermally synthesized	3 °C/min 600 °C 2 h	3 °C/min 1320 °C 2 h	~ 96			275	~ 15 – 17	Kirigami-Origami structures	[69]
BCZT	1 °C/min 1500 °C 2 h							Free standing pillars	[84]
BCZT	1 °C/min 800 °C 2 h	3 °C/min 1350 °C 2.5h	~ 92 – 93	256 – 1046	0.021 – 0.022	~ 62 – 100	4.11 – 4.56	Log-pile	[51]
BaTiO₃	1 °C/min 600 °C 1 h	5 °C/min 1350 °C 3 h	~ 94 – 98	~ 1700 – 2000		165 – 200		Bending bars	[70]
BaTiO₃	5 °C/min 600 °C 1 h	5 °C/min 1250 °C 2 h	~ 67.94 – 85.24	~ 1333.07 – 2250		~ 112.2 – 204.61		Hollow cylinder	[58]
BaTiO₃	5 °C/min 600 °C 1 h	5 °C/min 1250 °C 2 h	66.95 – 86.75	> 2200		135 – 200			[59]
BaTiO₃ doped La, Mn PTC	2 °C/min 350 °C	2 °C/min 1350 °C 2 h	> 99					Honeycomb, square grid, Circular, Elliptical, Square, Rectangular, Graded porous	[71]
PZT	3 °C/min 175 °C, 285 °C, 345 °C, 600 °C, Each step 1 h	3 °C/min 1250 °C 4 h	96.89	1621	0.031	342.6		Wood pile, Helical twentytetrahedral, Cylinder	[85]
BaTiO₃		1150 °C						Radial array, Periodic lattice	[49]
BaTiO₃		2.8 °C/min 1340 °C 1 h						Radial lattice, Linear lattice	[50]
Bi₂Mo₂O₉	1 °C/min 100 °C, 200 °C, 300 °C, 400 °C, 500 °C, Each step 2 h	3 °C/min 640 – 670 °C 2 h	86 – 93	~ 24.5 – 35.7	~ 0.0004 – 0.0006			Honeycomb	[60]
BaTiO₃	4 °C/min 600 °C 2 h	4 °C/min 1250 °C 2 h	70.25 – 89.97	1560.2 – 2391.6		175 – 244.5		Dense disc and rectangle	[61]
PZT	5 °C/min 650 °C 1 h	10 °C/min 1250 °C 6 h	~ 90 – 94.9	~ 4132	~ 3.4 %	678		Dense rectangle	[77]
PZT	325 °C, 500 °C, Each step 1 h	1250 °C 2 h	98.36			265		Woodpile structure bent into annulus or twisted to spiral	[72]
PIN-PMN-PT, BaTiO₃ platelet	0.1 °C/min 375 °C 9 h	10 °C/min 1050 °C 0h	95			420 – 480		Lattice structure	[91]
BaTiO₃, SrTiO₃, BaZrO₃Ni	350 °C 2 h	N ₂ + 200 ppm H ₂ : 5 °C/min 1350 °C 1 h		1247				Square array	[92]
Nb, Ca, Co- doped BaTiO₃	1 °C/min 600 °C 4 h	3 °C/min 1100 °C 4 h	~ 95	~ 1800	~ 0.52 %	~ 260		Disc	[80]
Titanium isopropoxide, MDEA, glycerol, water, BaO	10 °C/h 300 °C 2 h	60 °C/h 1250 – 1350 °C 20 h	94 – 96	1900		159	5.4	Cylindrical object	[73]
BaTiO₃	(i) 2 °C/min 200 °C, 500 °C, Each step 30 min (ii) 2 h	5 °C/min 800 °C, 2 °C/min 1200–1300 °C		462 – 858		201 – 312	1.7 – 2.3	Wood-pile	[88]
PZT	1 °C/min 170 °C, 250 °C, 375 °C, 600 °C, Each step 1 h	3 °C/min 1250 °C 4 h	97.8					Wood-pile	[83] ^c
BaCO₃, TiO₂	1 °C/min 500 °C, 600 °C, Each step 2 h	1 °C/min 1300 °C 2h, 5 h, 20 h	~ 94	2870 – 4120	0.033	290 – 360		Complex architectures	[93]
		1 °C/min 1300 °C 5h, Step cooling: 1 °C/min 1200 °C, 1100 °C, 1000		4380	0.02	420			

(continued on next page)

Table 8 (continued)

Feedstock	Debinding conditions	Sintering conditions	Density (%)	Dielectric constant, ϵ_r	Dielectric loss, $\tan\delta$	Piezoelectric coefficient, d_{33} (pC/N)	Polarization, P_f ($\mu\text{C}/\text{cm}^2$)	Printed structure	Reference
PZT	1 °C/min 600 °C 2 h	5 °C/min 1250 °C 2 h	98					Scaffolds	[54] ^c
PZT95/5 prepared from Pb_3O_4 , TiO_2 , ZrO_2 , Nb_2O_5	1 °C/min 600 °C 2 h	2 °C/min 1330 °C 2 h	83 ± 2	328		33.4 ± 0.4		3D periodically distributed porous structure	[94]
PNZT	2 °C/min 450 °C 3 h	950 – 1050 °C 5 h	60	1265	> 0.04			Square component	[75]
Li, Sb and Ta-doped KNN		3 °C/min 1050 °C, 1100 °C, 1130 °C, 2 h	98	1775		280	18.8	Wood pile	[95]
BaTiO ₃	5 °C/min 650 °C 1 h	5 °C/min 1100 °C, 1200 °C, 1300 °C, 1400 °C, 3 h	52.5 – 65.3	1580 – 4730	< 0.033	128 – 200		Dense square	[86]
PZT	600 °C 3 h	1250 °C 2 h		~ 1005 – 1533		~ 352 – 382		Hierarchical porous structure	[98]
PZT	3 °C/min 600 °C 2 h	3 °C/min 1275 °C 2 h	~ 98.8					3D periodic structure, V-shaped test structure, 3D radial structure, Porous lattice	[56]
BaTiO ₃	Debinding and sintering in a single step using different rapid sintering techniques		~ 72 – 95					Log-pile	[79] ^d

A generalized representation for heating rates is as follows: XX °C/min YY °C ZZ h ; where XX denotes heating rate, YY denotes the debinding/sintering temperature, and ZZ denotes the holding time. This representation has been followed in the subsequent Tables 9 – 11 as well.

^c Sintered samples were embedded in epoxy for the electrical measurements, hence the properties are not reported.

^d Different rapid sintering techniques employed were: ultra-fast high temperature sintering, pressureless spark plasma sintering and fast firing.

In the debinding/sintering condition, if atmosphere is not mentioned it is in ambient air.

well when depositing struts at different angles. On the other hand, in DIW the presence of the cooling fan is not mandatory and it may distort the structure or hinder the fine tuning of the rheological properties.

Most of the difficulties listed above may be overcome by employing vat photopolymerization. Overhanging structures can be printed quite easily, as the uncured resin provides support during the curing process. The resolution can be of the order of few microns (10 – 100 μm). This means it is practically possible to print fine structures with high resolution. On the other hand, printing large structures (similar to extrusion-based techniques) is quite difficult by this approach, especially considering the limited build volume and the time it takes to print with such fine resolution.

Prominent structures for transducer applications that have been produced using VP are circular/square/rectangular arrays with protruding pillars or features, specifically designed to enhance the performance of the device (Fig. 48(a-f)) [146,147,168,171,179,180,186,224]. The shape of the protruding features can be more flexible, in contrary to the traditional machining methods which could usually shape into square or rectangular features. In addition, the resolution of the protruding feature can be decreased down to the order of microns (Fig. 48(c, f)). To add to the architectural complexity, the pillars can be inclined at certain desired angles (Fig. 48(f)) [171]. Transducers with several other geometries and configurations have also been reported (Fig. 48(g-i)) [177,188]. The ability to fabricate overhanging structures are validated in several studies by printing a hollow cube like structure [146,147].

As a proof of concept, often TPMS (Triply periodic minimal surface) structures are employed to validate the flexibility of the printing process (Fig. 49(a-d)) [143,157,158,163,167,169,172,184]. For instance, a P-type TPMS structure with high geometrical porosity (70 %) was fabricated for energy harvesting applications (Fig. 49(e)). Notably, the design and porosity can be adjusted easily to meet specific needs. Often such TPMS structures are embedded in epoxy for practical applications

[139,157,158].

The samples fabricated with powder-bed based AM techniques (BJ and SLS) often suffer from low resolution and rough surfaces, as shown in Fig. 50. As a result, these techniques are not used to fabricate piezoelectric device to the same extent as the other techniques evaluated in this work. Most of the published articles only report the fabrication of simple shapes, such as discs as shown in Fig. 50(d), as required for carrying out the electrical measurements [192,194,198,199]. Scaffolds with a possible application in bone tissue engineering were successfully fabricated using BT/HA (Fig. 50(a)) [197]. In addition, TPMS and lattice structures were reported to confirm the viability of complex architectures (Fig. 50(b-c)) [192].

Until now, various complex structures that are fabricated with different AM techniques have been discussed, with more details provided in Tables 8 – 11. Following this, Table 12 highlights the applications of fabricated piezoelectric ceramics across various fields, demonstrating the versatility and potential of these devices.

In summary, the choice of a specific AM technology depends on the specific requirements of the application. For fabricating large components with relatively simple designs, extrusion-based AM techniques are suitable, although there may be a compromise in resolution. In such cases, BJ can also be considered. However, this technique suffers from various disadvantages, including high surface roughness, low green strength and high residual porosity, to name a few. On the other hand, if the design is highly complex with fine features, VP is the most suitable option. The final decision to select the appropriate AM technology depends on factors such as availability and end-use requirements. It is essential to weigh the advantages and disadvantages of each technology to ensure the desired outcomes for the specific application envisioned.

5. Conclusions and outlook

In this review, a comprehensive assessment of the main features,

Table 9

Post-processing conditionings and functional properties of samples fabricated with fused filament fabrication.

Feedstock	Debinding	Sintering	Density (%)	Dielectric constant, ϵ_r	Dielectric loss, $\tan\delta$	Piezoelectric coefficient, d_{33} (pC/N)	Polarization, P_r ($\mu\text{C}/\text{cm}^2$)	Printed structure	Reference
PZT	30 °C/h 500 °C 4 h							Dome and radial actuator, 2–2 ceramic polymer composite	[99]
PZT-5H	10 °C/h 550 °C	1285 °C 1 h	94 – 96	~ 3100	~ 0.025	~ 650 pC/N			
PZT-5H	550 °C	1285 °C 1 h	94	2300	0.035	620 – 1270			
PZT	30 °C/h 500 °C 2 h	3.5 °C/min 1285 °C 1 h		700		290		2–2 annular ring, 3–3 ladder structure	[120]
PZT	60 °C/h 200 °C, 10 °C/h 550 °C 4 h	3.5 °C/min 1285 °C 1 h	7.7 g/cc	3340	0.023	664 ± 4		2–2 transducer	[122]
BiT powder, BiT platelets	550 °C	1100 °C 1 h							[102]
PZT	10 °C/h 550 °C	1285 °C 1 h						Tube array, Radial, spiral and bellow actuators	[103]
PZT-5HSpray dried	1 °C/min 350 °C 1 h, 1.5 °C/min 550 °C 2 h, 3.5°C/min 800 °C 1 h	3.5 °C/min 1285 °C 1 h						Ladder structure	[104]
PZT	Wick debinding 125 °C, 150 °C, 175 °C, 200 °C, 225 °C	10 K/min 1200 °C 2 h		~ 1873	~ 7.2 %	~ 270		Filament	[118]
BaTiO ₃	3 °C/min 200 °C,	1350 °C 5 h						scaffold	[131]
PZT	0.25 °C/min 500 °C 2 h	1200 °C 2 h							
BaTiO ₃	3 °C/min 200 °C, 0.25 °C/min 500 °C 2 h	1350 °C 5 h 1200 °C 2 h		906 – 1372 297 – 1177		107 – 127 202 – 273	2.9 – 3.5 6.2 – 25.5	Open and offset scaffold	[116]
PZT	600 °C for 60h: Binder removal by capillary forces	150 °C/h 1250 °C 2 h	7.71 g/cc	2060	0.0191	477		Concentric rings	[123]
BaTiO ₃	2 °C/min 180 °C 30 min, 0.3 °C/min 300 °C 60 min, 0.5 °C/min 550 °C 60 min, 3 °C/min 1000 °C 60 min	10 °C/min 1200 – 1350 °C 2 h	~ 58 – 92	1228 – 1472	0.010 – 0.012	196 – 221	11.39 – 12.33	Porous gyroid, log-pile, honeycomb, dense disc, triangular	[113]
PZT 5 H	30 °C/h 550 °C 2 h	3.5 °C/min 1285 °C 1 h						2–2 annular ring, 3–3 ladder structure, C ring actuator	[133]

advantages, and disadvantages of the most commonly used AM technologies employed for fabricating piezoceramic components, such as direct ink writing (DIW), fused filament fabrication (FFF), vat photopolymerization (VP), binder jetting (BJ), and selective laser sintering (SLS) was carried out. AM is one of the most efficient and rapid prototyping techniques that enables the fabrication of complex structures with high precision and desired geometry. Especially concerning piezoelectric ceramics, the functional properties can be easily tailored by the geometry of the fabricated component. This is where 3D printing takes an additional leap forward with respect to other conventional processing techniques, providing a high degree of customization to the users. There are more than 120 publications in the past 20 years related to the above-mentioned technologies, with most of them being reported in the past 2–3 years. These observations suggest that these AM technologies have not been commercialized yet and further developments are required. Additionally, there is a clear trend towards lead-free compositions, which is evident from Fig. 1(c) where the number of papers published on BT surpasses those on lead-based compositions. However, the piezoelectric and ferroelectric properties of lead-based compositions remain significantly superior to those of other materials reported. For instance, as detailed in Tables 8, 9, 10 and 11, the d_{33} values for most lead-based compositions exceed 350 pC/N, with the highest reported value reaching 1270 pC/N. In contrast, compositions

based on BT or KNN have d_{33} values up to a maximum of 250 pC/N. Even though researchers are employing various methods such as doping and texturing, the properties still remain significantly below those of lead-based compositions. Nevertheless, with advancements in technology and materials innovation, there is a hope that lead-based materials could eventually be completely replaced by lead-free compositions. Such an accomplishment can be only fulfilled with continuous research and development of the lead-free compositions.

To ensure the successful fabrication of defect-free components, it is essential to carefully formulate a printable feedstock with desired rheology, which in turn affects the piezoelectric performance of the fabricated devices. A typical printable feedstock is composed of ceramic powders, dispersants, solvents, binders and several other additives, depending on the printing technique to be used. concerning VP and DIW of piezoceramic materials, thanks to the availability of affordable and economical printers. The progress of the FFF technology applied to ceramics over the last several years is directly related to the only minor modifications to the cheap and open-source printers that can extrude polymeric materials that are required. While most of the recent advancements in this area have focused on composite polymer-ceramic piezoelectric materials, there is still a great opportunity for optimization and exploration in the realm of pure ceramic devices. On the other hand, because of the inferior product quality and performance, the

Table 10

Post-processing conditionings and functional properties of samples fabricated with vat photopolymerization.

Feedstock	Debinding conditions	Sintering conditions	Density (%)	Dielectric constant, ϵ_r	Dielectric loss, $\tan\delta$	Piezoelectric coefficient, d_{33} (pC/N)	Polarization, P_r ($\mu\text{C}/\text{cm}^2$)	Printed structure	Reference
PZT-5H	700 °C	1 °C/min 1200 °C	≥ 95	2000					[176]
PMNT	1 °C/min 600 °C 1 h	3 °C/min 1250 °C 1.5 h	97.8 (7)			620 (40)		Hollow spherical cell transducer	[177]
PZT 5 H BaTiO ₃	1 °C/min 700 °C <u>Argon:</u> 600 °C 3 h	1330 °C 4 – 6 h	95 – 98 93.7	1350	0.012	160	2.2 – 7	Transducer 64 pillar annular segment transducer	[178] [179]
BaTiO ₃	<u>Argon:</u> 1 °C/min 200 °C, 300 °C, 400 °C, 500 °C, Each step 0.5 h, 600 °C 3 h	3 °C/min 1200 – 1500 °C 4 h	~ 95	920	0.07	87	~ 12	Annular segment transducer array	[168]
KNN	<u>Argon:</u> 1 °C/min 100 °C, 200 °C, 300 °C, 350 °C, 400 °C, 500 °C, 600 °C, Each step 2 h; <u>Air:</u> 800 °C 3 h	3 °C/ min 1050 – 1150 °C 3 h	~ 92	2150	0.08	170	12.1	Annular array for ultrasonic transducer	[180]
BaTiO ₃	0.5 °C/min 600 °C 2 h	1290 °C 2 h	5.52 – 5.68 g/cc	1829 – 2276	0.036 – 0.094	96 – 166	28.5	Ultrasonic array	[181]
PZT-5A	1 °C/min 280 – 500 °C	1 °C/min 1200 °C 2 h	97 – 98						[164]
BaTiO ₃	<u>Nitrogen:</u> 600 °C 5 h	1320 °C 3 h	~ 95	2762	0.016	163		9 rod transducer, Hollow cube, Annular ring Hollow cube, Transducer with pillars	[146]
BaTiO ₃	<u>Nitrogen:</u> 1 °C/min 300 °C, 0.15 °C/min 400 °C 3 h, 0.15 °C/min 500 °C, 1 °C/min 600 °C 3 h	1300 °C, 1320 °C, 1330 °C 2 h	~ 95.89 – 98.06	~ 2749 – 4423	0.0128 – 0.0188	146 – 206			[147]
BaTiO ₃	<u>Nitrogen:</u> 1 °C/min 200 °C, 300 °C, 400 °C, 450 °C, 500 °C, 600 °C, Each step 1 h; <u>Air:</u> 1 °C/min 450 °C, 600 °C, Each step 2 h	1330 °C 2 h	~ 61.98 – 95.32	948	0.023	168.1	13.1	Octet truss, Gyroid	[139] ^e
PZT	<u>Argon:</u> 1 °C/min 100 °C, 200 °C, 300 °C, 350 °C, 400 °C, 500 °C, 600 °C, Each step 2 h; <u>Air:</u> 800 °C 3 h	1200 °C 3 h	6.09 – 6.92 g/cc	2417	0.025	525	17.3	Annular array	[171]
BaTiO ₃	<u>Air/ Vacuum:</u> 3 °C/min 150 °C 30 min, 1 °C/min 200 °C 30 min, 0.35 °C/min 300 °C, 400 °C, 500 °C, Each step 1 h, 0.35 °C/min 600 °C 2 h	1300 – 1400 °C 2 – 4 h	86.93 – 90.25	1965	0.017	200		Circular disc	[159]
BaTiO ₃	<u>Inert:</u> 1 °C/min 150 °C, 0.5 °C/min 150 – 200 °C 3h, 1 °C/min 200 – 350 °C, 0.5 °C/min 350 – 400 °C 3h, 1 °C/min 400 – 420 °C; <u>Air:</u> 460 °C 3 h	1320 °C 2 h	~ 91 – 95.4	1543	0.0185	180	5 – 10.9	Complex structures	[148]
BaTiO ₃	<u>Nitrogen:</u> 0.5 °C/min 300 °C, 400 °C, 450 °C, 500 °C, 600 °C, 700 °C, Each step 1 h;	3 °C/min 1210 – 1330 °C 2 h	~ 87.54 – 95.32	~ 718 – 1512		~ 108.2 – 168.1	7.59 – 20.25	Disc, FCC-structured	[157]

(continued on next page)

Table 10 (continued)

Feedstock	Debinding conditions	Sintering conditions	Density (%)	Dielectric constant, ϵ_r	Dielectric loss, $\tan\delta$	Piezoelectric coefficient, d_{33} (pC/N)	Polarization, P_r ($\mu\text{C}/\text{cm}^2$)	Printed structure	Reference
BCZT	Air: 1 °C/min 450 °C, 600 °C, 800 °C, Each step 2 h Argon: 1 °C/min 150 °C, 0.3 °C/min 180 °C, 400 °C, Each step 2h, 0.5 °C/min 600 °C 2h; Air: 3 °C/min 600 °C 2h	3 °C/min 1450 – 1525 °C 4 h	~ 93.28 – 95.88	4800	0.025	430	14.38		[149] ^f
BaTiO ₃	12 °C/h 200 °C 1 h, 6 °C/h 300 °C 1 h, 12 °C/h 700 °C 1 h	100 °C/h 1300 °C 1 h	62 – 98	837 – 2426	0.01 – 0.068	5 – 148		Cylinder or rectangular	[182]
KNNLN-Er	Vacuum: 600 °C 4 h, 800 °C 4 h	1120 °C 4 – 8 h	89.6 – 93			97		Disc	[183] ^g
PZT	Argon: 0.2 °C/min 200 °C, 310 °C, 395 °C, Each step 2 h	1250 °C 2 h	~ 77.8 – 89.51	1522 – 2196	0.025 – 0.029	254 – 373	24.78 – 35.56	Calibration model	[150]
PMN-PT, BT templates		2.5 °C/min 1200 °C, 1235 °C 4 h	~ 93	2218	0.077	652	19.5	Square	[162]
BaTiO ₃	Nitrogen: 2 °C/min 100 °C, 200 °C, Each step 2h, 1 °C/min 250 °C, 300 °C, 340 °C, 380 °C, 400 °C, Each step 3h, 2 °C/min 500 °C, 600 °C 2 h; Air 600 °C 3h	3 °C/min 1300 °C 3h	78.74 – 91.69 %	5631 – 10009 at T _c	~ 0.03 at T _c	73 – 151	8.8 – 17.4	Disk	[151]
BaTiO ₃	Nitrogen: 1 °C/min 200 °C, 300 °C, 400 °C, 450 °C, 500 °C, 600 °C, Each step 1 h; Air: 1 °C/min 450 °C, 600 °C, Each step 2 h	3 °C/min 1250 °C, 1300 °C, 1330 °C, 1350 °C 2 h	~ 90.02 – 95.39	978	0.038	215 ± 13	16.656	TPMS, cylinder	[158]
PZT	Argon: 0.2 °C/min 190 °C, 368 °C, 465 °C, Each step 2 h; Air: 600 °C 2 h	3 °C/min 1250 °C 2 h	~ 85.45 – 87.12	1970 – 2113	0.0256 – 0.0267	340 – 365	32.67 – 34.40	Disk	[152]
BCZT	Argon: 1 °C/min 150 °C, 0.3 °C/min, 180 °C, 400 °C, Each step 2 h, 0.5 °C/min 600 °C 2h; Air: 3 °C/min 600 °C 2h	3 °C/min 1450 – 1525 °C 4 h	~ 93.14 – 96.58	4323	0.011	525	14.50	Gyroid	[184] ^h
BaTiO ₃ , BT platelets	Inert: 1 °C/min 150 °C, 0.5 °C/min 150–200 °C 3 h, 1 °C/min 200 °C – 350 °C, 0.5 °C/min 350 – 400 °C 3 h, 1 °C/min 400 – 420 °C; Air: 460 °C 3 h	3 °C/min 1250 °C, 1275 °C, 1300 °C, 1325 °C 3 h		~ 1867	0.037	275	14.88	TPMS	[163]
PZT	0.2 °C/min 250 °C, 375 °C, 480 °C 2h	3 °C/min 1250 °C 2 h	~ 68 – 83.12	868 – 1911	0.027 – 0.032	129 – 308	15.75 – 29.68	TPMS	[172]
BaTiO ₃	Vacuum: 1 – 8 °C/min 600 °C; Air: 0.5 – 4 °C/min 800 °C	2 °C/min 1450 °C				211		TPMS	[143]
KNN	Argon: 1 °C/min 150 °C, 0.2 °C/min 410 °C, 600 °C Each step 2 h; 1100 °C 6 h	5 °C/min 1070 °C, 1080 °C, 1090 °C,	90.11	460.43 ± 6.05	0.12 ± 0.01	113.67 ± 2.49	19.94(30 kV/cm)	Scaffolds	[144]

(continued on next page)

Table 10 (continued)

Feedstock	Debinding conditions	Sintering conditions	Density (%)	Dielectric constant, ϵ_r	Dielectric loss, $\tan\delta$	Piezoelectric coefficient, d_{33} (pC/N)	Polarization, P_r ($\mu\text{C}/\text{cm}^2$)	Printed structure	Reference
BaTiO ₃ -xBaSnO ₃	Air: 3 °C/min 600 °C 2 h Inert: 1 °C/min 150 °C, 0.5 °C/min 150 – 200 °C 3 h, 1 °C/min 200 – 350 °C, 0.5 °C/min 350 – 400 °C 3 h, 1 °C/min 400 – 420 °C; Air: 460 °C 3 h	1400 °C 4 h	1767–10532		17 – 283		1.1 – 11.92	Complex structures	[167]
BaTiO ₃		1350 °C 4 h	~ 99					Honeycomb	[185] ⁱ
Barium acetate, Titanium (IV) isopropoxide, Acetic acid, Acrylic acid	5 °C/min 90 °C, 250 °C, 385 °C, 655 °C, 900 °C, ramp held for 1 h	5 °C/min 1330 – 1500 °C 1 h	87 ± 1 – 93 ± 1					Complex structures	[175]
PZT 5 H	Vacuum: 600 °C 3 h; Air: 650 °C 3 h	1250 °C 2 h	6.94 – 7.00 g/cc	760 – 1390	0.020 – 0.021		212 – 345	Ceramic array	[186]
PZT855	Argon: 1 °C/min 600 °C 3 h; Air: 600 °C 3 h	1100 °C 3 h	94.7			583	32.4	Micro-curved stave elements, Hemispherical transducers, Helical element, Cylindrical concentric annular arrays, Lattice sensor	[188]
PZT	Argon + Air	1250 °C 3 h	72.98 – 91.43	1256 – 2364	0.0241 – 0.0302	189 – 399	20.44 – 39.72	Complex structures	[145]
BaTiO ₃	Argon: 0.25 °C/min 400 °C, 460 °C, 550 °C 2 – 3 h, 800 °C 2 h 3 h	1 °C/min 450 °C 4 h, 2 °C/min 1000 °C, 1320 °C	95	1770	0.029	201	18.5	TPMS structures: schwarz, gyroid, I-WP, bodycentred cubic lattice	[140]
PZT, PMMA	Vacuum: 0.5 – 2 °C/min 100 °C, 200 °C, 300 °C, 400 °C, 500 °C, Each step 2 h; Air: 600 °C 4 h	1200 °C 2 h	~ 6.36 – 6.55 g/cm ³					Cylinder	[189]
BaTiO ₃	Vacuum: 0.5 °C/min 600 °C 4 h; Air: 1 °C/min 800 °C 4 h	3 °C/min 800 °C, 1 °C/min 1320 °C 2 h	94.52 – 95.51	1805 – 2019	0.02 – 0.03	107 – 218	6.31 – 11.05	Square	[190]
Sm-PMN-PT	Argon: 0.5 °C/min 140 °C, 380 °C, 420 °C, Each step 1 h, 1 °C/min 600 °C 1 h	2.5 °C/min 600 °C, 1220 °C, Each step 2 h	92 – 98	4733 – 6452	0.0430 – 0.0434		1080 – 1230	Hollow cylinder, TPMS: Gyroid, Schwarz_P, Schwarz_D	[141]
BCZT	Nitrogen: 1 °C/min 300 °C, 0.5 °C/min 500	1450 °C 3 h	718 – 1603			382 – 570		Gyroid	[165]

^e Best properties reported for the sample with relative density of 95.32 %.^f Best properties reported for the sample with sintered at 1500 °C.^g Best properties reported for the sample with a holding time of 6 h.^h Best properties reported for the sample doped with 1.5 mol.% CuO (relative density 96.58 %).ⁱ Sintered samples were embedded in epoxy for the electrical measurements; hence the properties are not reported.

binder jetting technology still remains largely unexplored.

The key distinction between additively manufactured and conventionally manufactured piezoceramics, beyond the unique structural complexity achievable with AM, lies in the differences in density and microstructure in the sintered components. In conventional methods, the application of pressure during the shaping process with limited or without the use of any binder helps in achieving high densities with fine microstructures. In contrary, the residual porosity from the debinding process affects the electrical properties of additively manufactured components in a negative way. Increasing the sintering temperature helps in enhancing the densification process but at the expense of grain

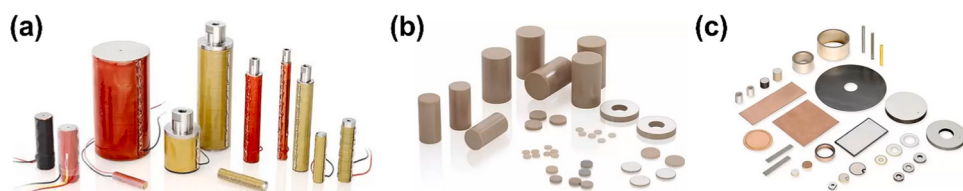
growth.

Tables 2 – 6, and 8 – 11 provide an overview of different feedstocks used to fabricate piezoelectric ceramics with complex geometries using AM technologies, along with their sintering and post-processing conditions, as well as their electrical properties. They complement the discussion and assist the reader in formulating their own approach to the fabrication of devices using the AM approach. Examining the tables, one can clearly notice the differences between various additive manufacturing (AM) technologies and their capabilities. If one is concerned about resolution with a limited object size, vat photopolymerization (VP) is the best choice. For applications where resolution

Table 11

Post-processing conditionings and functional properties of samples fabricated with binder jetting.

Feedstock	Debinding	Sintering	Density (%)	Dielectric constant, ϵ_r	Dielectric loss, tan δ	Piezoelectric coefficient, d_{33} (pC/N)	Polarization, P_r ($\mu\text{C}/\text{cm}^2$)	Printed structure	Reference
BaTiO ₃	10 °C/min 600 °C 0.3 h 1330 °C, 1400 °C 4h	10 °C/min 1260 °C, 1320 °C 1 h	1.3 – 1.6 g/cc	8.62 – 6.23					[196]
BaTiO ₃ Hydroxyapatite	300 °C 1 h, 500 °C 2 h	600 °C 3 h, 1000 °C 2 h, 1320 °C 1 h	~ approx. 50 % open porosity			3.08 pC/N		Scaffolds (Interconnected cylinder)	[197]
BaTiO ₃	10 °C/min 600 °C 20 min 1330 °C, 1400 °C 4 h	10 °C/min 1260 °C, 1330 °C, 1400 °C 4 h	41.4 – 65.2 (60 % binder saturation)	~ 50 – 630	~ 0.01 – 0.81	13.23 – 74.1 pC/N		Dense rectangle	[195]
KNN	2.5 °C/min 1130 °C 2 h	~ 29.5 – 56				~ 74.1 – 89.9		Discs, Triangle with hole at the centre	[191]
BaTiO ₃	10 °C/min 650 °C 60 min 1300 °C, 1350 °C, 1400 °C, Each temperature 2 h, 4 h, 6 h	10 °C/min 1300 °C, 1350 °C, 1400 °C, Each temperature 2 h, 4 h, 6 h	~ 82 – 93	750 (Coarse), 811 (Fine)	0.0553 (Coarse), 0.1159 (Fine)	118 (Coarse), 183 (Fine)		Disc, Lattice structure	[194] ^j
BaTiO ₃	600 °C 60 min	2 °C/min 1200 – 1400 °C 2 h	56 – 66.8	371, 411	< 3 %	105, 110		Disc	[198] ^k
BCZT	600 °C 60 min	1400 – 1500 °C, Each temperature 2 h, 4 h, 8 h, 10 h	~ 74 – 91	1909	1.9	152		Disc, TPMS (Gyroid and Schwarz)	[192]
PZT-N	470 °C 4 h	1200 or 1250 °C 2 h	~ 45 – 60	400 – 482		291 – 319		Disc	[199]
BaTiO ₃	7.5 °C/min 650 °C 1 h	10 °C/min 1250 °C 6 h	36.77	581.6 (Parallel), 698 (Perpendicular)		113 (Parallel), 152 (Perpendicular)			[200] ^l
BaTiO ₃	1260 – 1400 °C			~ 50 – 650					[193] ^l
PZT						468.5 pC/N (Parallel), 541.4 (Perpendicular)			

^j Here, coarse refers to the properties reported for that specific powder fraction, and similarly for fine.^k Best properties reported for the sample sintered at 1250 °C.^l Parallel and perpendicular refers to the orientation in which the values are measured.**Fig. 44.** Commercially used piezoelectric components. (a) Soft PZT for actuators and sensors; (b) Hard PZT for ultrasonic transducers; and (c) Lead-free BNT (Bismuth sodium titanate) suitable for transducers. Note these commercial products are all produced using conventional shaping methods [236].

is not the primary criterion, extrusion-based AM techniques can be used, with fused filament fabrication (FFF) being particularly well-suited for its better shape retention ability owing to the thermoplastic nature of the binder. However, preparing the filaments for the FFF process is time-consuming and requires proper attention. On the other hand, with direct ink writing (DIW), the ink preparation step is relatively easy when compared to FFF. In addition, the limited amount of binder used in DIW is a significant advantage when it comes to the post processing stages. Regardless of the method, samples fabricated with these technologies exhibit acceptable piezoelectric and ferroelectric properties. In contrast, samples fabricated with binder jetting (BJ) exhibit poor resolution and low properties, making them unacceptable for many applications.

However, this technology involves high production rate and volume, when compared to other AM technologies reported in this review paper. The choice of AM technology should consider not just the resolution and ease of material preparation but also the specific material properties required for the application, post-processing requirements and the overall cost and scalability of the manufacturing process.

Despite significant advancements in AM technologies for piezoelectric device production, there are some unresolved issues that must be addressed before widespread use and commercialization can occur. These concerns need attention and should be regarded as the goals for future growth and development of the field.

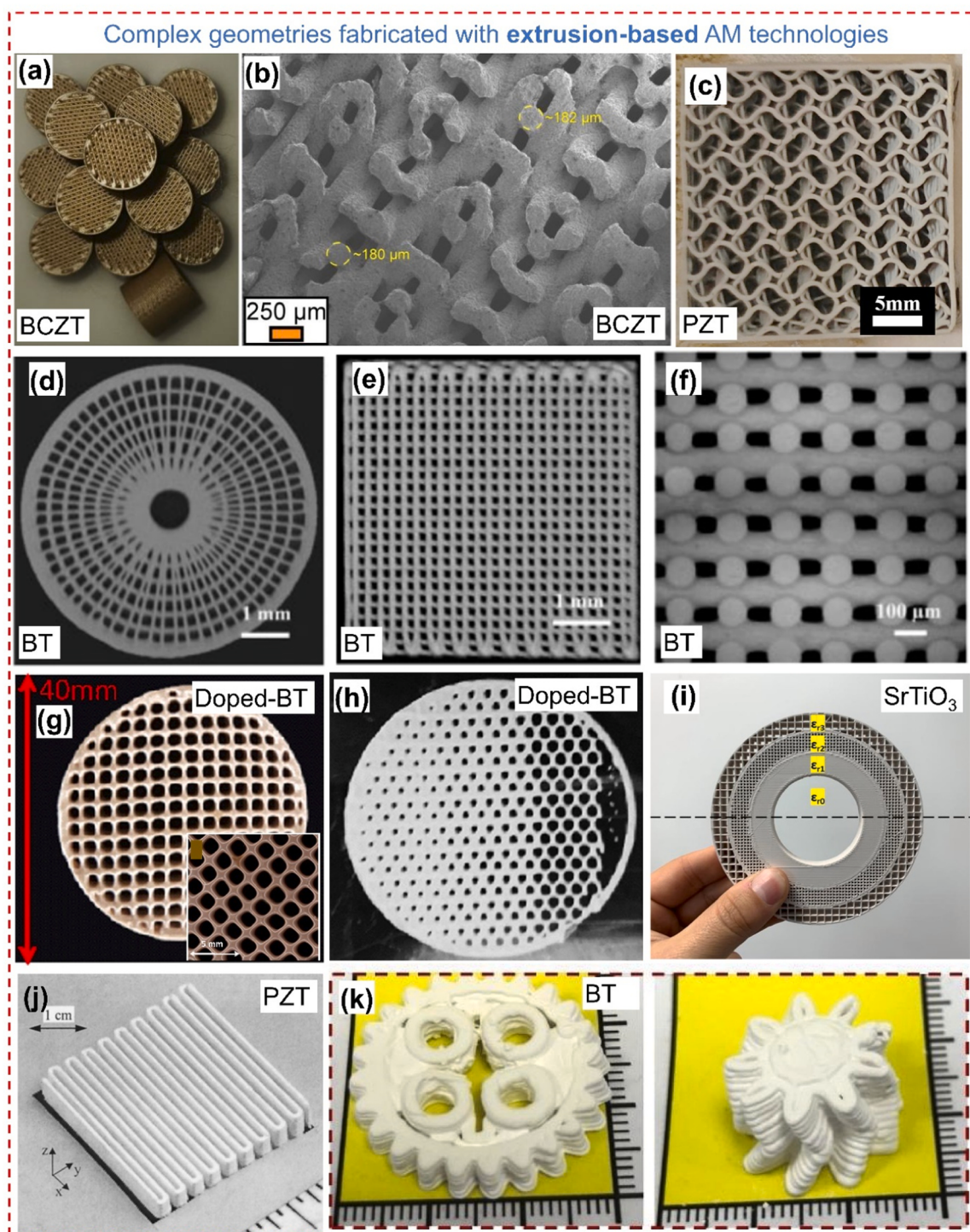


Fig. 45. Optical images of: (a-b) BCZT scaffolds for bone graft substitute with the corresponding SEM image of the fracture surface [97], (c) Helical twenty tetrahedral structure fabricated using PZT ceramics [85], (d) 3D radial array, and (e-f) 3D periodic lattice printed using a $100\text{ }\mu\text{m}$ nozzle with BT nanoparticle ink, with the cross-sectional over-view [49], (g) Sintered BT honeycomb heating element. The inset shows a magnified optical micrograph of a sintered square grid structure [71], (h) 3D printed green sample with graded porous structure for possible use in heating elements [71], (i) Fresnel zone plate lens fabricated using FFF [107], (j) PZT array [122], and (k) BT green body from milled precursors with complex architectures [93].
 (a-b) [97] Open access article distributed under the terms of the Creative Commons CC BY license. Reproduced from Ref.: (c) [85], (g-h) [71], (i) [107], (j) [122], and (k) [93], with permission from Elsevier. (d-e) [49], with permission from John Wiley and Sons.

(i) Use of simple piezoceramic powders

Pure piezoceramic powders, such as PZT, BT, KNN, PNN-PZT and PMNT, have been used for AM in the majority of the articles that have been published so far. There are few studies concerning doped

compositions. This means such formulations are still beyond the reach of the AM technologies. In such a scenario, where the trend is to shift from lead-based to lead-free piezoceramics, it is necessary to employ doped compositions in lead-free formulations to enhance the functional properties. The best doped composition should be shared to the industrial

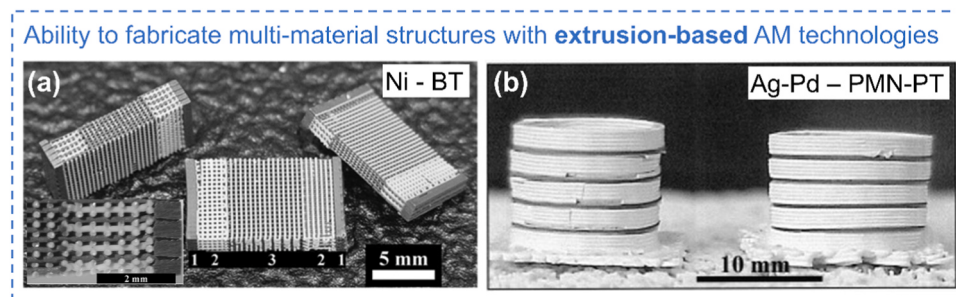


Fig. 46. (a) Isometric view of multilayer Ni-BT structures. The inset shows the cross-section [92]. (b) Multilayer tube actuators made of PMN-PT and electrode materials (silver-palladium) [238].

Reproduced from Ref.: (a) [92], with permission from John Wiley and Sons. (b) [238], with permission from Elsevier.

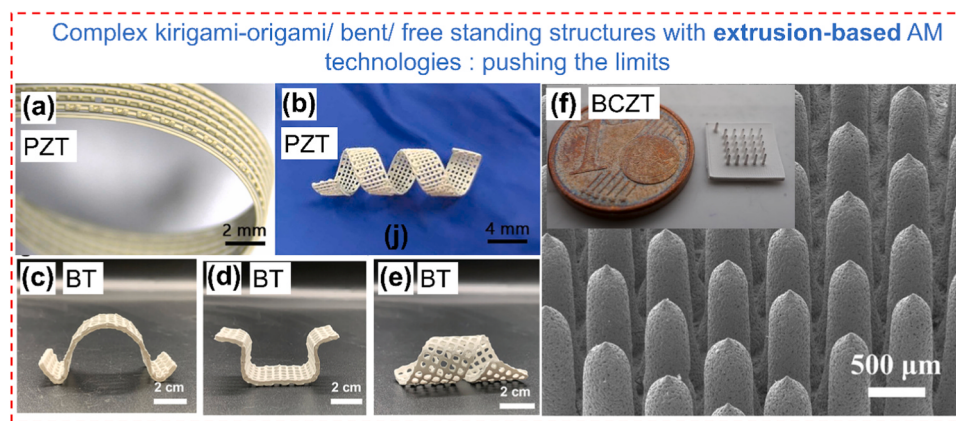


Fig. 47. Optical photos of printed green bodies (a) Bent into an annular structure, and (b) Twisted into ribbon spiral [72]. (c-e) Photographs of sintered kirigami-origami structures with different configurations [69]. (f) Representative optical image of the free-standing pillars with their corresponding SEM micrographs [84].

Reproduced from Ref.: (a-b) [72], and (f) [84], with permission from Elsevier. (c-e) [69] Open access article distributed under the terms of the Creative Commons CC BY license.

partners for production in bulk quantities.

(ii) Limited use of texturing

It is widely established that texturing through templated grain growth significantly enhances the piezoelectric properties. The manufacturing technique for the platelets, on the other hand, is highly time demanding and calls for high levels of control over the stoichiometry. For such reasons, the production of the platelet powders has not been widely commercialized yet. Moreover, achieving a fully aligned distribution of platelets within additively manufactured parts using currently available technologies is still a challenge. This restricts the further usage of the concept of texturing in the field of AM.

(iii) Ability to fabricate multi-material structures

The concept of multi-material fabrication using piezoceramics is still in its early stages. The integration of various piezoceramic materials or piezoceramics with other materials, such as metals, polymers or other ceramics, can be made possible by multi-material AM. Enhanced sensitivity and better mechanical properties are two examples of enhanced performance attributes that may result from this.

(iv) Hybridization of technologies

Hybridization in AM refers to the integration and exploitation of the unique advantages of several production techniques. To enhance the quality of piezoceramics, one possible approach is to combine Direct Ink

Writing (DIW) with stereolithography (SLA) to create components with enhanced flexibility. Such hybridization has been recently reported by several authors [240,241] and could be translated to piezoceramic components as well.

(v) Limited size

AM techniques are often restricted by the build volume of the available printers. This is particularly challenging when a large component is desired. For example, the debinding of large components is time-consuming and can lead to delamination or warping during the thermal treatment process. Internal stresses during the printing can also increase when fabricating large components. In addition, the time required to print large structures can lead to an economic constraint. There is often a compromise between the dimensions of the component and the level of resolution or detail that can be attained. When dealing with larger components, it may be necessary to use thicker layers in order to keep the printing time reasonable. However, this might result in a loss of detail and a less smooth surface quality.

(vi) Rapid post processing

Efficient post-processing techniques are crucial for enhancing productivity and minimising the production time. Rapid sintering techniques, such as spark plasma sintering, ultra-fast high temperature sintering etc., which aim at decreasing the sintering temperature and time drastically, have not been well implemented yet. The microstructure is strongly affected by the heating and cooling rates, with rapid